Journal of Translational Medicine

RESEARCH

Open Access

Multi-omics-driven discovery of invasive patterns and treatment strategies in CA19-9 positive intrahepatic cholangiocarcinoma

Delin Ma[1,2,3,4†], Pengcheng Wei[1,2,3,4†], Hengkang Liu[5], Jialing Hao[1,2,3,4], Zhuomiaoyu Chen[1,2,3,4], Yingming Chu[6], Zuyin Li[1,2,3,4], Wenzai Shi[7], Zhigao Yuan[8], Qian Cheng[1,2,3,4], Jie Gao[1,2,3,4], Jiye Zhu[1,2,3,4*] and Zhao Li[1,2,3,4*]

Abstract

Background Intrahepatic cholangiocarcinoma (ICC) is a malignant tumor with a poor prognosis, predominantly CA19-9 positive. High CA19-9 levels correlate with increased aggressiveness and worse outcomes. This study employs multi-omics analysis to reveal molecular features and identify therapeutic targets of CA19-9 positive ICC, aiming to support individualized treatment.

Methods Data from seven clinical cohorts, two whole-exome sequencing cohorts, six RNA sequencing/microarray cohorts, one proteomic cohort, 20 single-cell RNA sequencing samples, and one spatial transcriptome sample were analyzed. Key findings were validated on tissue microarrays from 52 ICC samples.

Results CA19-9 positive ICC exhibited poorer OS (median 24.1 v.s. 51.5 months) and RFS (median 11.7 v.s. 28.2 months) compared to negative group (all $P < 0.05$). Genomic analysis revealed a higher KRAS mutation frequency in the positive group and a greater prevalence of IDH1/2 mutations in the negative group (all $P < 0.05$). Transcriptomic analysis indicated upregulated glycolysis pathways in CA19-9 positive ICC. Single-cell analysis identified specific glycolysis-related cell subclusters associated with poor prognosis, including Epi_SLC2A1, CAF_VEGFA, and Mph_SPP1. Higher hypoxia in the CA19-9 positive group led to metabolic reprogramming and promoted these cells' formation. These cells formed interactive communities promoting epithelial-mesenchymal transition (EMT) and angiogenesis. Drug sensitivity analysis identified six potential therapeutic drugs.

Conclusions This study systematically elucidated the clinical, genomic, transcriptomic, and immune features of CA19-9 positive ICC. It reveals glycolysis-associated cellular communities and their cancer-promoting mechanisms, enhancing our understanding of ICC and laying the groundwork for individualized therapeutic strategies.

Keywords Intrahepatic cholangiocarcinoma, CA19-9, Multi-omics, Glycolysis, Hypoxia

†Delin Ma and Pengcheng Wei have contributed equally to this work as co-first authors.

*Correspondence:
Jiye Zhu
gandanwk@vip.sina.com
Zhao Li
lizhao@pku.edu.cn
Full list of author information is available at the end of the article

Graphical Abstract

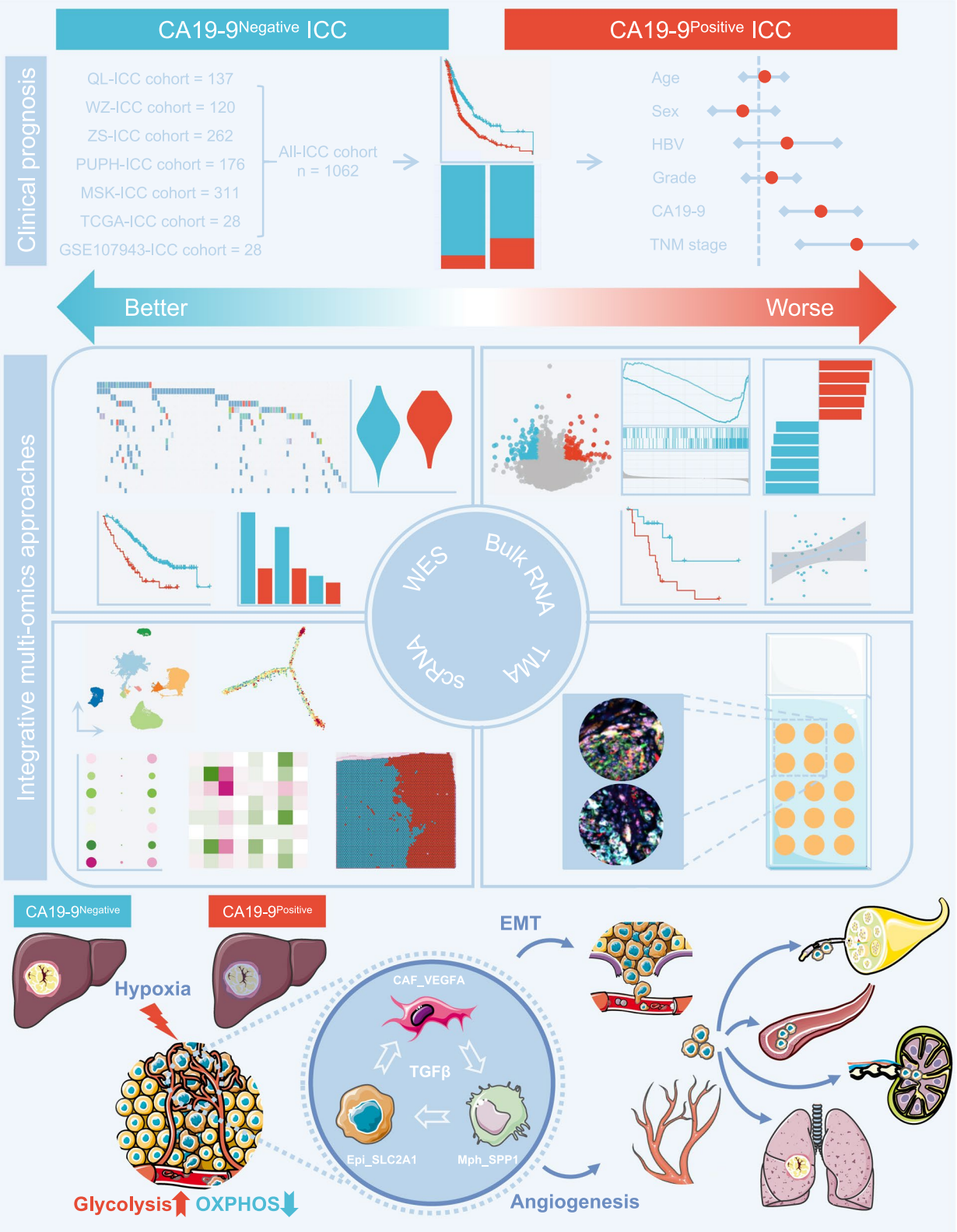

Background

Cancer, as a complex and diverse group of diseases, poses a significant challenge to global health and profoundly impacts human health and quality of life. According to data from the World Health Organization, cancer is one of the leading causes of death worldwide [1]. Despite substantial progress in cancer treatment in recent years, with many promising drugs and therapies emerging, fully conquering cancer remains a long and challenging journey [2–4].

Cholangiocarcinoma (CCA) is a category of malignant tumors originating from intra- and extrahepatic biliary epithelial cells exhibiting diverse biliary differentiation patterns. The classification of CCA is based on its location within the biliary tree and includes intrahepatic cholangiocarcinoma (ICC), perihilar cholangiocarcinoma (PCC), and distal cholangiocarcinoma (DCC) [5]. ICC arises from secondary biliary epithelial cells in the liver above the confluence of the right and left hepatic ducts. It is the second most common liver malignancy after hepatocellular carcinoma (HCC), accounting for 10%-15% of primary liver cancers [6, 7]. A notable increase in the incidence of ICC has been observed globally in recent years, with exceptionally high rates in Asia surpassing those in Europe and the United States [8]. ICC is linked to a multitude of risk factors, such as bile duct stones, viral hepatitis, cirrhosis, and liver fluke infection [9, 10]. The tumor's heterogeneity, invasive nature, and the tendency for slow onset and rapid progression often result in a lack of early, distinctive symptoms. This characteristic leads to a majority of patients being diagnosed at an advanced stage, presenting limited treatment options and generally unfavorable outcomes; for patients with early-stage ICC, radical surgical resection remains the potentially curative treatment. However, even with surgery, the 5-year survival rate hovers at a modest 25–40%, significantly lower than that observed in HCC patients [11, 12]. In advanced ICC, treatments like chemotherapy are often limited by side effects and drug resistance [13–15]. Current research must unravel the molecular mechanisms of ICC and its clinical prognosis while focusing on developing individualized treatments and "therapeutic-diagnostic integration" strategies to improve patient outcomes and quality of life [2, 3, 16].

Carbohydrate antigen 19-9 (CA19-9), also known as the salivary acidified Lewis, a blood group antigen, is a crucial tumor marker associated with the prognosis of various adenocarcinomas, including biliary tract tumors, gastrointestinal cancers, and pancreatic cancers [17]. CA19-9 expression depends on the Lewis antigen phenotype. About 5–10% of the Lewis (a-b-) population is CA19-9 hyposecretory and virtually incapable of synthesizing CA19-9 [18]. Elevated CA19-9 levels are seen in benign conditions like stone biliary obstruction and primary sclerosing cholangitis [19, 20]. Despite these limitations, CA19-9 remains the most commonly used tumor marker in ICC studies and is considered a reliable biomarker at all stages of ICC diagnosis and treatment. High preoperative serum CA19-9 levels are significantly associated with poorer survival in ICC patients and can predict lymph node metastasis and postoperative prognosis, according to the literature [21]. Studies show that CA19-9-positive (>37 U/mL) ICC patients exhibit more aggressive biological behavior and poorer clinical outcomes than CA19-9-negative patients [22, 23]. However, specialized and effective treatments for CA19-9-positive ICC patients are lacking, with surgical resection being the primary option. Therefore, it is urgent to reveal the molecular features, signaling pathway activities, and gene expression patterns of CA19-9-positive ICC through multi-omics analysis, providing more in-depth information for individualized treatment and prognostic assessment.

Glycolysis is a critical pathway in tumor cell metabolism that is upregulated to provide cancer cells with the energy and metabolic intermediates necessary for rapid proliferation. This metabolic reprogramming supports tumor cell growth and correlates with anti-apoptotic properties, further contributing to tumor invasiveness and metastatic ability [24, 25]. Hypoxia is a prominent feature of many solid tumors and a common cause of tumor progression and poor treatment outcomes [26]. Several studies also suggest that CA19-9-positive ICC may have a more hypoxic environment [27].

Existing literature still needs a comprehensive multi-omics integrated analysis of the mechanisms underlying poor prognosis in CA19-9 positive ICC patients, hindering deeper exploration of its mechanisms. In this study, we integrated multi-omics data—including genomics, transcriptomics, proteomics, and single-cell RNA sequencing (scRNA-seq)—to systematically elucidate the clinical, genomic, transcriptomic, and immune microenvironment characteristics of CA19-9 positive ICC for the first time, revealing its pro-cancer mechanisms. This research bridges the gap in current studies and provides a novel theoretical basis for individualized treatment strategies for ICC.

Methods

Data collection

In this study, a patient sample was positive if the preoperative serum CA19-9 levels were greater than 37U/ml; otherwise, it was considered negative. The clinical data includes seven cohorts, all including serum CA19-9 levels. Among these cohorts, the QL-ICC (n=137) [28], WZ-ICC (n=120) [29], ZS-ICC (n=262) [30], MSK-ICC

(n = 311) [31], TCGA-ICC (n = 28) [32], and GSE107943-ICC (n = 28) [33]cohorts were obtained from previous studies. Ethical approval information can be found in the original publication. In addition, we also collected a PUPH-ICC cohort consisting of 176 ICC patients who underwent surgical treatment at Peking University People's Hospital from 2015 to 2024. The ethics committee approved clinical data collection, and informed consent was obtained from patients. The whole-exome sequencing (WES) data consists of two cohorts: the ZS-ICC cohort (n = 262) and the MSK-ICC cohort (n = 311). Transcriptomics data, including RNA sequencing (RNA seq) and chip microarray data, consists of six cohorts, namely ZS-ICC (n = 253), TCGA-ICC (n = 32/40, patient/total sample), GSE107943-ICC (n = 30/57), GSE76297-ICC (n = 92/185) [34], GSE32225-ICC (n = 149/155) [35], and GSE26566-ICC (n = 104/169) [36] cohorts. The proteomic data similarly comes from the ZS-ICC cohort (n = 216). The scRNA-seq data comes from a previous study published by our team [37], and we finally selected 10 CA19-9 positive and 10 CA19-9 negative samples. In addition, the spatial transcriptome data was obtained from Wu et al.'s study, which contained one ICC sample [38]. The detailed description of these cohorts can be found in Supplementary Table 1, 2, and 3.

Functional annotation analyses

In this study, we used of clusterProfiler R package (v4.6.2) [39] to perform the functional annotation of the interested genes in this study. Hallmark gene sets, gene ontology (GO), and the Kyoto encyclopedia of genes and genomes (KEGG) were used to assess the relevant functional categories.

Gene set enrichment analysis (GSEA)

GSEA was performed using the clusterProfiler package (v4.6.2). The alteration in gene expression between groups was calculated, and a gene list was generated based on the fold change values. The GSEA () function determined the normalized enrichment score (NES) and P-value of Hallmark pathway gene sets.

ScRNA-seq analysis

In this study, raw scRNA-seq data were preprocessed using the CellRanger software (v 3.1) to generate an expression matrix, which was subsequently processed by the Seurat R package (v 4.4.0) [40]. The cell filtration process mainly follows the method of Xue et al. [37], but at the mitochondrial gene expression threshold, we set the upper limit to 20%. After filtering, we employed the DoubletFinder R package (version 2.0.3) with default parameters to exclude doublet cells. We then used the NormalizeData() function to normalize the data, followed by the ScaleData() function using pre-selected 3000 highly variable genes (HVGs). Subsequently, the batch effects across different samples were removed by Harmony R package (version 0.1.1) [41]. We performed principal component analysis (PCA) using the RunPCA() function for dimensionality reduction. Finally, we employed the RunUMAP() function, in conjunction with the first 30 Harmony-corrected components, to generate two-dimensional UMAP plots that visually represent the intercellular relationships.

Cell clustering and annotation

In the present study, we employed a two-step approach for cell annotation. Initially, cell clustering was performed using the FindClusters() function from the Seurat package, with the resolution parameter set to 0.1, and the Louvain algorithm was utilized to execute preliminary clustering. Subsequently, based on established cellular markers, cells were categorized into eight major cell types, which include Epithelial cells (marked by EPCAM, KRT19), Stromal cells (COL1A1, DCN), T/NK cells (CD3D, CD3E), Endothelial cells (VWF, PECAM1), Macrophages/Dendritic cells (Mph/DC, CD68, C1QA), Neutrophils (S100A9, FCGR3B), B/Plasma cells (CD79A, MS4A1), and Mast cells (KIT, TPSAB1). We applied distinct resolution parameters within each major cell type in the second clustering round for further subclassification. For epithelial cells, the resolution parameter was adjusted to 0.25, facilitating the identification of seven epithelial cell clusters. The resolution for stromal cells was set to 0.3, and eight stromal cell clusters were identified. The resolution parameter for Mph/DC cells was set to 0.5, and nine Mph/DC clusters were identified. The resolution for endothelial cells was set to 0.2, and seven endothelial cell clusters were identified. Finally, the cluster marker genes were identified by FindMarkers() or FindAllMarkers() functions, while the signature scores were calculated by the AddModuleScore() function.

Quantitative analysis of cell cluster enrichment

To assess the differential enrichment of various cell clusters between CA19-9 positive and negative groups, this study adopted the methodology from a previous study [42]. Specifically, we estimated the expected occurrence counts for the cell cluster using the chi-square ($\chi 2$) test. After that, we calculated the ratio of the actual observed cell counts to the expected counts, also known as the Ro/e score, defined by the formula: Ro/e = Observed / Expected. Briefly, Ro/e > 1 indicates enrichment of the cell cluster in the CA19-9 positive group, while < 1 signifies enrichment in the negative group.

Copy number variation (CNV) analysis

In this study, we utilized the infercnv R package (version v1.14.2) [43] to analyze copy number variations in epithelial cells. Initially, we employed the InfercnvObject() function, inputting the count's matrix of epithelial cells extracted from the Seurat object to create an inferCNV analysis object. A reference sample was constituted by randomly selecting 5,000 non-epithelial microenvironmental cells, which were used to estimate the copy number status of epithelial cells. Finally, we executed the run() function with a cutoff value 0.1 to calculate the CNV values for each epithelial cell.

Single-cell metabolism analysis

In this study, we employed the scMetabolism R package (version v 0.2.1) developed by Wu et al. [44] to analyze metabolic activities at the single-cell level. By utilizing the sc.metabolism.Seurat() function, we computed the activity of individual cells across various metabolic pathways. While executing of this function, we specified the method parameter as "AUCell" and set the metabolism. type parameter to "KEGG".

Cell development trajectory analysis

In this study, we inferred cell development trajectories using Monocle2 R package (version v2.26.0) [45]. A corresponding CellDataSet object was generated from the Seurat object using the newCellDataSet() function. We selected 3000 HVGs for trajectory inference. Subsequently, data dimension reduction was performed using the DDRTree algorithm within the reduceDimension() function, and cells were ordered along the trajectory based on the dimension reduction results.

Cell–cell communication analysis

This study employed the CellChat R package (version 1.6.1) [46] and its integrated ligand-receptor interaction database to perform inferential analysis on cell–cell communication. The CellChatDB.human database covers various communication categories, including "Secreted Signaling," "ECM-Receptor," and "Cell–Cell Contact." Using the createCellChat() function, we constructed a CellChat object and assessed intercellular communication with default parameters. Furthermore, we employed functions such as netVisual_heatmap(), netVisual_circle(), and netVisual_bubble() to visualize the detailed interactions and communication probabilities between cellular clusters.

The R package NicheNet (v2.0.4) [47] was used to infer interaction mechanisms in Epi_SLC2A1, CAF_VEGFA, and Mph_SPP1. For ligand and receptor interactions, the genes expressed in more than 10% of the cells of the clusters were considered. The top 200 upregulated genes in Epi_SLC2A1 and the top 400 in CAF_VEGFA and Mph_SPP1 were extracted for paired ligand-receptor activity analysis. The make_heatmap_ggplot () function was used to display the regulatory pattern.

Glycolysis-related cellular communities (GRCC) signature

We identified GRCC signature through scRNA-seq data. Initially, we employed the FindMarkers() function to calculate DEGs within the Epi_SLC2A1, CAF_VEGFA, and Mph_SPP1 cell clusters, respectively. Subsequently, the top 50 genes from each cell cluster were selected and merged. During the merging process, duplicate genes were retained only once.

Spatial transcriptome data analysis

This study employed the Seurat R package (version v4.4.0) to process the gene expression matrix generated from spatial transcriptome data. Initially, each spot was normalized using the SCTransform() function to ensure the data's comparability. Subsequently, we used RunPCA() for dimensionality reduction and set the resolution to 0.1 to define clusters. Using the AddModuleScore() function, we calculated the cellular signature scores for each spot. The SpatialFeaturePlot() function was used to generate the spatial feature plot.

Drug sensitivity analysis

Drug sensitivity analysis was conducted using the oncoPredict R package (version v0.4). The input data comprised gene expression profiles of human cancer cell lines (CCL) sourced from the Cancer Cell Line Encyclopedia (CCLE) (https://depmap.org/portal/). In contrast, corresponding drug sensitivity data were obtained from the Cancer Therapeutics Response Portal (CTRP) v2 (https://portals.broadinstitute.org/ctrp.v2.1/) [48]. Using the calcPhenotype() function, we estimated each drug's area under the curve (AUC), where lower AUC values indicate higher drug sensitivity. Subsequently, we utilized the limma R package (version v3.54.2) to analyze differences in drug response between GRCC and other cell types. Potential candidate drugs targeting GRCC were identified by reducing AUC values ($log2FC < -0.10$ and $P < 0.05$). Additionally, within the ZS-ICC cohort, we selected candidate drugs with significantly reduced AUC in CA19-9 positive patients that showed a significant negative correlation with GRCC signature scores (correlation coefficient $r < -0.3$ and $P < 0.05$). Finally, the intersection of these analyses yielded the final candidate drugs.

Immunohistochemical (IHC) and multiplexed immunofluorescence (mIF) staining

The tissue microarray (TMA) containing 52 ICC tissue samples was used for IHC and mIF. The tissues were derived from the surgical resection specimens of Peking University People's Hospital from 2021 to 2024 with informed consent and ethical approval from the ethics committees. The clinical information for the TMA patients is shown in Supplementary Table 4.

The TMA slides were baked at 65 °C overnight and then were deparaffinized and rehydrated using Xylene, 100% ethanol, and 95% ethanol. Next, these slides were boiled in citrate buffer at 100 °C for 18 min to retrieve antigen. Subsequently, endogenous peroxidase activity was blocked by incubating the slides in 3% H_2O_2 solution for 30 min. The BSA prevented nonspecific antibody binding for 30 min at room temperature. Then, these slides were incubated at four°C overnight with a Hypoxia-inducible factor 1-alpha primary antibody (HIF1-α, Cat#ab51608, Abcam). After three washes with TBST, the slides were further incubated with an HRP-conjugated secondary antibody for one hour at room temperature. Finally, the slides were stained with DAB and then counterstained with hematoxylin. The images of IHC were obtained using an ICX41 microscope (SOPTOP) and analyzed using ImageJ software (ImageJ-win64).

The TMA slides were deparaffinized, rehydrated, antigen retrieved, and blocked following the IHC process. Subsequently, the slides were incubated with primary antibody and corresponding Horseradish peroxidase (HRP)-conjugated secondary antibody. Repeat the above steps until all markers have been stained. Finally, the nuclei were stained with DAPI, and the slides were sealed with an anti-fluorescence quenching agent. The primary antibodies used in this study included Cytokeratin 19 (CK19, Cat#10712-1-AP, Proteintech), Osteopontin (Cat#25715-1-AP, Proteintech), Glucose Transport Protein 1 (GLUT1, Cat#21829-1-AP, Proteintech), Alpha-Smooth Muscle Actin (αSMA, Cat#ab5694, Abcam), CD68 (Cat#76437S, CST), and Vascular Endothelial Growth Factor (VEGF, Cat#ET1604-28, HUABIO). The images of mIF were recorded by a Pannoramic SCAN II scanner (3D HISTECH) and were analyzed using ImageJ software (ImageJ-win64).

Statistical analysis

In this study, the Student's t-test and the Mann–Whitney U-test were used to compare the means of two groups; the Pearson or Spearman correlation test was used to test the relation between numerical variables. For categorical variables, the χ2 test was employed. In the Kaplan–Meier (KM) survival analysis, differences between the two groups were evaluated using the log-rank test. Variables with P-values less than 0.1 in the univariate COX regression analysis were selected and included in the multivariate COX regression analysis. All statistical analyses in this study were performed using R software (version v4.2.2). Results with a two-tailed P-value less than 0.05 were considered statistically significant.

Results

The status of CA19-9 is associated with the aggressive phenotype and poor prognosis of ICC patients.

To further evaluate the clinical significance of CA19-9 in ICC, this study collected data from seven medical centers comprising 1062 ICC patients and conducted a retrospective analysis on the relationship between CA19-9 status and clinical phenotypes. Preliminary analysis revealed a specific association between CA19-9 levels, aggressive phenotype and poor prognosis in ICC patients across multiple clinical cohorts (Supplementary Fig. 1A-AK). Although some cohorts did not achieve statistical significance due to limited sample sizes, the overall trend was evident. Subsequently, we merged all patient data into a combined cohort for further analysis. The results showed that the overall survival (OS) and recurrence-free survival (RFS) of CA19-9 positive patients were significantly lower than those of negative patients (Fig. 1A, B). Moreover, compared to CA19-9 negative patients, the CA19-9 positive had significantly increased proportions of perineural invasion, vascular invasion, lymph node metastasis, and distal metastasis (Fig. 1C–F). Multivariate COX analysis further confirmed that the positive status of CA19-9 is an independent risk factor on both OS and RFS (Fig. 1G, H, Supplementary Table 5, 6). These findings support the notion that the positive status of CA19-9 is closely related to the aggressive phenotype and poorer prognosis in ICC patients.

The genomic characteristics between CA19-9 positive and negative ICC patients.

We ffirst compared the top 50 mutated genes in the ZS-ICC and MSK-ICC cohorts (Fig. 2A, Supplementary Fig. 2A). We found that only ten genes were shared between the two cohorts (highlighted in red), suggesting differences in the mutational landscape of different ICC populations. In both datasets, the critical driver mutation genes, including TP53, KRAS, IDH1/2, and BAP1, showed high mutation frequencies in the rankings, further confirming their essential role in ICC development. When comparing the mutation frequencies of 10 genes shared by two cohorts in the two groups, we observed that IDH1/2, PBRM1, and BAP1 mutation frequencies were generally higher in the CA19-9 negative group. In contrast, the KRAS gene is generally higher in the

CA19-9 positive group. The mutation frequency distribution of the remaining six genes in the two cohorts is inconsistent (Fig. 2B, Supplementary Fig. 2B).

Next, we compared the differences of all mutated genes between the two groups and found that only KRAS and IDH1/2 were significant in both cohorts (Fig. 2C, Supplementary Fig. 2C). Furthermore, we investigated the potential impact of KRAS and IDH1/2 mutations on OS and RFS. The results indicate that KRAS mutations are associated with poorer OS and RFS (Fig. 2D, Supplementary Fig. 2E, F). ICC patients with IDH1/2 mutations exhibit better OS and RFS trends (Fig. 2E, Supplementary Fig. 2G,H). Considering that mutation burden is usually associated with poor prognosis of tumors, we further compared the tumor mutation burden (TMB) between the two groups. However, the differences in TMB in both cohorts were not statistically significant (Fig. 2F, Supplementary Fig. 2I). Collectively, our findings suggest that there are distribution differences of crucial driver genes between CA19-9 positive and negative ICC patients, and these phenomena may underlie the molecular basis for the clinical prognostic differences.

Transcriptome and proteomic analysis unveiled an enhanced glycolytic activity in CA19-9 positive patients

Through differential expression analysis, we identified 836, 343, and 710 significant DEGs ($P < 0.05$ and $|logFC| > 0.5$) between the CA19-9 positive and negative groups in ZS-ICC, TCGA-ICC, and GSE107943-ICC cohorts (Fig. 3A–C), respectively. Subsequently, we used GSEA to reveal the differences in Hallmark pathways between the two groups (Fig. 3D–F). An intersection analysis was conducted to pinpoint robust differentially activated pathways. The results indicated that the Hallmark glycolysis, Hallmark P53, Hallmark estrogen response late, and Hallmark allograft rejection pathways were significantly activated in all cohorts (Fig. 3G, Supplementary Table 7). In contrast, no shared downregulated pathways were obtained in the intersection analysis (Supplementary Fig. 3A). Of the four upregulated pathways, the Hallmark glycolysis pathway was associated with poorer prognosis across all three cohorts (Fig. 3H–J). In comparison, the prognostic impact of the other three pathways was less consistent (Supplementary Fig. 3B-D). Hallmark glycolysis scores were positively correlated with serum CA19-9 levels in all three cohorts (Fig. 3K–M). Considering that the transcriptomic data may not reflect the actual changes in protein level, we further analyzed the proteomic data from the ZS-ICC cohort. The enrichment analysis on the upregulated proteins showed significant enrichment in multiple glycolysis-related pathways (Fig. 3N, O), which confirmed the upregulation of the glycolytic pathway in CA19-9 positive ICC patients. In the ZS-ICC cohort, the multivariate COX analysis indicated that the Hallmark glycolysis score was an independent prognostic risk factor (Supplementary Fig. 3E, Supplementary Table 8). Furthermore, the Hallmark glycolysis scores showed a significant tumor elevation compared to normal adjacent tissues in five independent cohorts, confirming its association with malignant characteristics (Supplementary Fig. 4A-E). Notably, patients with KRAS mutations exhibited higher Hallmark glycolysis scores (Supplementary Fig. 4F), suggesting that glycolysis may serve as an intermediate factor in KRAS-mediated malignant phenotypes of ICC. In conclusion, we confirm that the glycolytic pathway was excessive activation in CA19-9 positive patients, which may be responsible for their poorer prognosis.

ScRNA-seq successfully identified three cell clusters associated with enhanced glycolytic activity in CA19-9 positive ICC patients

We turned to single-cell analysis to investigate the critical cell subpopulations responsible for the rise in glycolytic activity. After strict quality control, we obtained 97,768 high-quality cells from 20 ICC samples (Fig. 4A, Supplementary Fig. 5A, B). All cells were further divided into nine major cell clusters (Fig. 4A, B), and each cluster was defined by marker genes described in our methods section (Supplementary Fig. 5C, Supplementary Table 9). By evaluating the glycolytic score of single cells, we found that epithelial cells, stromal cells, and Mph/DC are the main clusters of glycolytic active cells (Fig. 4D, E). The scMetabolism analysis also indicated that these three cell types exhibited the highest glycolytic metabolic activity (Supplementary Fig. 5D, E). In terms of cell count, these three cell types were also numerically abundant, further supporting their significant impact on overall glycolytic activity (Fig. 4C). Notably, we observed an increase in both the number and strength of interactions between

(See figure on next page.)

Fig. 1 Survival analysis and aggressive characteristics of CA19-9 positive ICC patients in combined cohort. **A**, **B** The KM curves show that patients in the CA19-9 positive group exhibit poorer OS (**A**) and RFS (**B**) in the combined ICC cohort. **C**–**F** The bar plots show the proportion differences of perineural invasion (**C**), vascular invasion (**D**), lymph node metastasis (**E**), and distal metastasis (**F**) between CA19-9 positive and negative groups in the combined ICC cohort. **G**, **H** The forest plots display the multivariate Cox regression result for OS (**G**) and RFS (**H**) in the combined ICC cohort. P-values were calculated using the Log-rank test in (**A**, **B**), the Chi-square test in (**C**–**F**), and the multivariate COX regression analysis in (**G**, **H**)

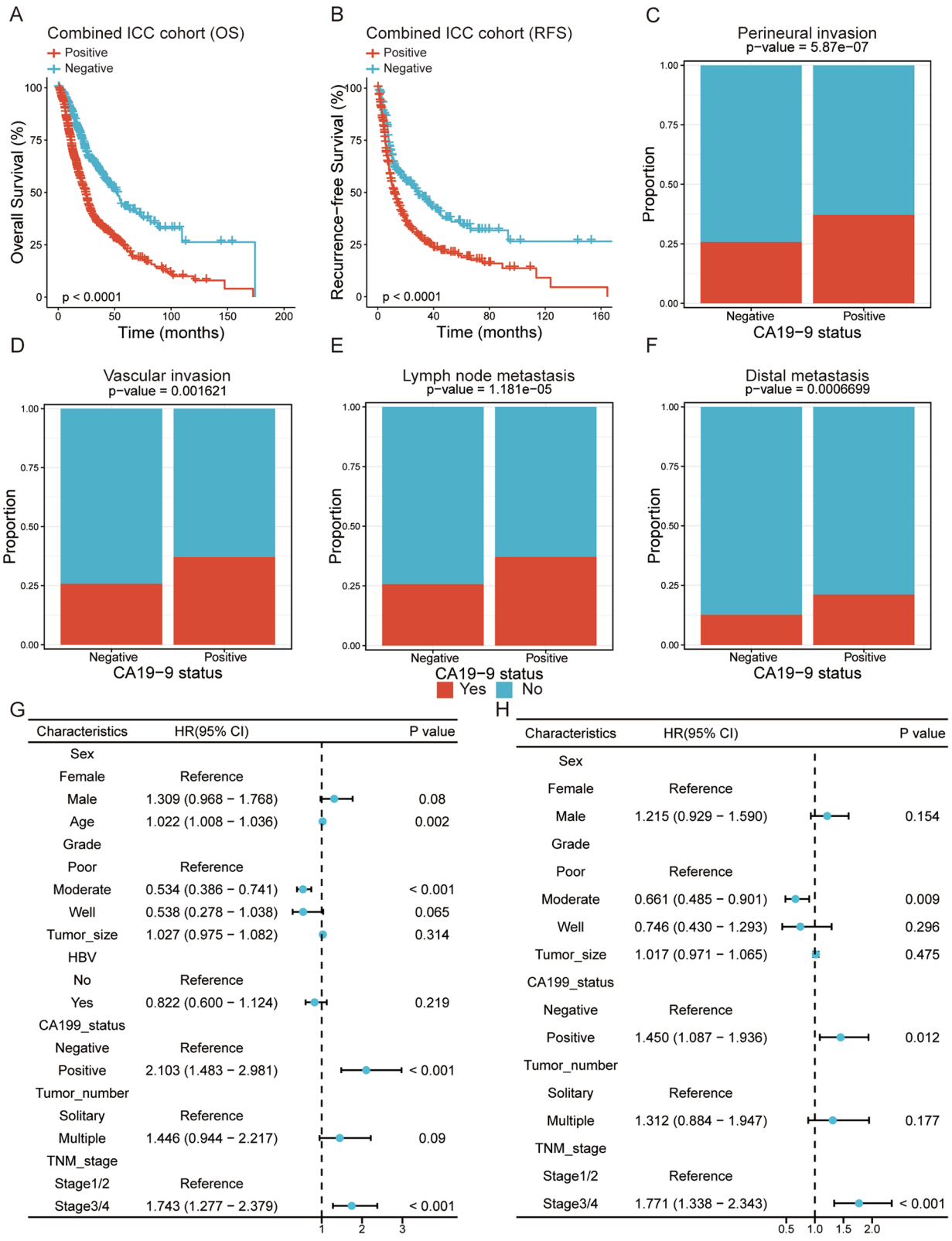

Fig. 1 (See legend on previous page.)

these three cell types and epithelial cells in the CA19-9 positive ICC (Fig. 4F, Supplementary Fig. 5F). Given the pivotal role of epithelial cells in tumor invasion and prognostic impact, these cell types with predominant glycolytic activities may play a vital role in the malignant progression of tumors.

Based on the above findings, we conducted a more in-depth analysis of these three cell types. Specifically, we subdivided the epithelial cells into seven subclusters, designated as Epi_SLC2A1, Epi_APOE, Epi_IGS15, Epi_RPS27, Epi_FOS, Epi_FCER1G, and Epi_Cycling (Fig. 4G, H, Supplementary Table 10). The distribution of these subclusters varies between CA19-9 positive and negative ICC patients, with the Epi_SLC2A1, Epi_IGS15, Epi_FCER1G, and Epi_Cycling being more prevalent in CA19-9 positive ICC patients (Fig. 4I, J). Through InferCNV analysis, we identified a high level of CNV in these seven clusters, supporting their identity as malignant cells (Supplementary Fig. 5G, H). Furthermore, by calculating the glycolytic pathway score and scMetabolism analysis, we noted that the Epi_SLC2A1 exhibits the highest glycolytic activity compared to all other epithelial cell subclusters (Fig. 4K, L). Additionally, GSEA analysis revealed marked upregulation of the Hallmark glycolytic pathway in the Epi_SLC2A1 (Fig. 4M). Critically, key enzymes in the glycolytic pathway, such as LDHA, HK2, and PKM, were also expressed at significantly higher levels in the Epi_SLC2A1 compared to other epithelial subclusters (Fig. 4N), further confirming its role as the primary executor of glycolytic activity among epithelial cells. In the ZS-ICC cohort, we observed that the Epi_SLC2A1 top 50 gene signature scores were significantly higher in the CA19-9 positive group compared to the negative group. Furthermore, groups with higher Epi_SLC2A1 signature scores were correlated with poorer OS. Additionally, we found a positive correlation between the Epi_SLC2A1 signature scores, the Hallmark glycolysis scores, and the serum CA19-9 levels (Fig. 4O).

We conducted a more in-depth analysis of these three cell types based on the above findings. The stromal cells were categorized into eight subclusters (Supplementary Fig. 6A, B, Supplementary Table 11), Mph/DC cells were further divided into seven macrophage subclusters and two DC subclusters (Supplementary Fig. 6H, I, Supplementary Table 12). Through Ro/e analysis, we observed differences in the distribution of these cell subclusters among different groups (Supplementary Fig. 6C, J). Using glycolytic pathway scores and scMetabolism analysis, we screened the CAF_VEGFA and Mph-SPP1 subgroups, which exhibited significant glycolytic activity in their respective cell populations (Supplementary Fig. 6D, E, K, L), and these two clusters were more likely to be distributed in CA19-9 positive ICC patients. The results of the GSEA analysis further confirmed the significant upregulation of glycolytic pathways in these two clusters (Supplementary Fig. 6F, M). In addition, both cell clusters highly express critical genes involved in glycolysis, including HK2, PKM, and SLC2A1 (Supplementary Fig. 6G, N). In the ZS-ICC cohort, the top 50 gene signature scores for these two cell clusters were significantly higher in CA19-9 positive patients, and the group with high signature scores was significantly associated with poorer prognosis. We also found a positive correlation between the signature scores of the two clusters, glycolysis pathway scores, and serum CA19-9 levels (Supplementary Fig. 6O, P).

We performed mIF on 26 ICC samples collected at our center to validate our analytical findings. The staining results indicated a higher cellular density of the Epi_SLC2A1, CAF_VEGFA, and Mph_SPP1 cell subclusters in the CA19-9 positive patient group (Fig. 5A–C). Statistical analysis further confirmed that the positive group's cell count per unit area was significantly increased compared to the negative group (Fig. 5D), which is consistent with the in silico results. Collectively, we successfully identified cell subgroups with enhanced glycolytic activity in epithelial cells, stromal cells, and Mph/DC cells. These subgroups are more prevalent in CA19-9 positive ICC patients and are associated with poorer prognosis.

Glycolysis-related cellular communities are associated with the aggressive phenotype and adverse prognosis in CA19-9 positive ICC

We utilized spatial transcriptome technology to explore the spatial distribution and interactions of the three cell subclusters within the tumor microenvironment. Firstly,

(See figure on next page.)

Fig. 2 Gene mutation pattern and tumor mutation burden of CA19-9 positive patients in the ZS-ICC cohort. **A** The waterfall plot shows the top 50 mutated genes in the ZS-ICC cohort. The genes marked in red are common to both cohorts. **B** The bar plot shows the mutation frequency differences of the ten shared high-ranked genes between CA19-9 positive and negative groups in the ZS-ICC cohort. ns: no significance. *P < 0.05. **C** The bar plot shows the genes with significant mutation frequency among all genes between CA19-9 positive and negative groups in the ZS-ICC cohort. Red represents a higher frequency in the positive group, while blue represents a higher frequency in the negative group. **D**, **E** The KM curves of OS between patients with and without KRAS (**D**) and IDH1/2 (**E**) mutations in the ZS-ICC cohort. **F** The violin plot shows the difference in tumor mutation burden between the CA19-9 positive and negative groups in the ZS-ICC cohort. P-values were calculated Using the Chi-square test in (**B**, **C**), the Log-rank test in (**D**, **E**), and the Student's t-test in (**F**)

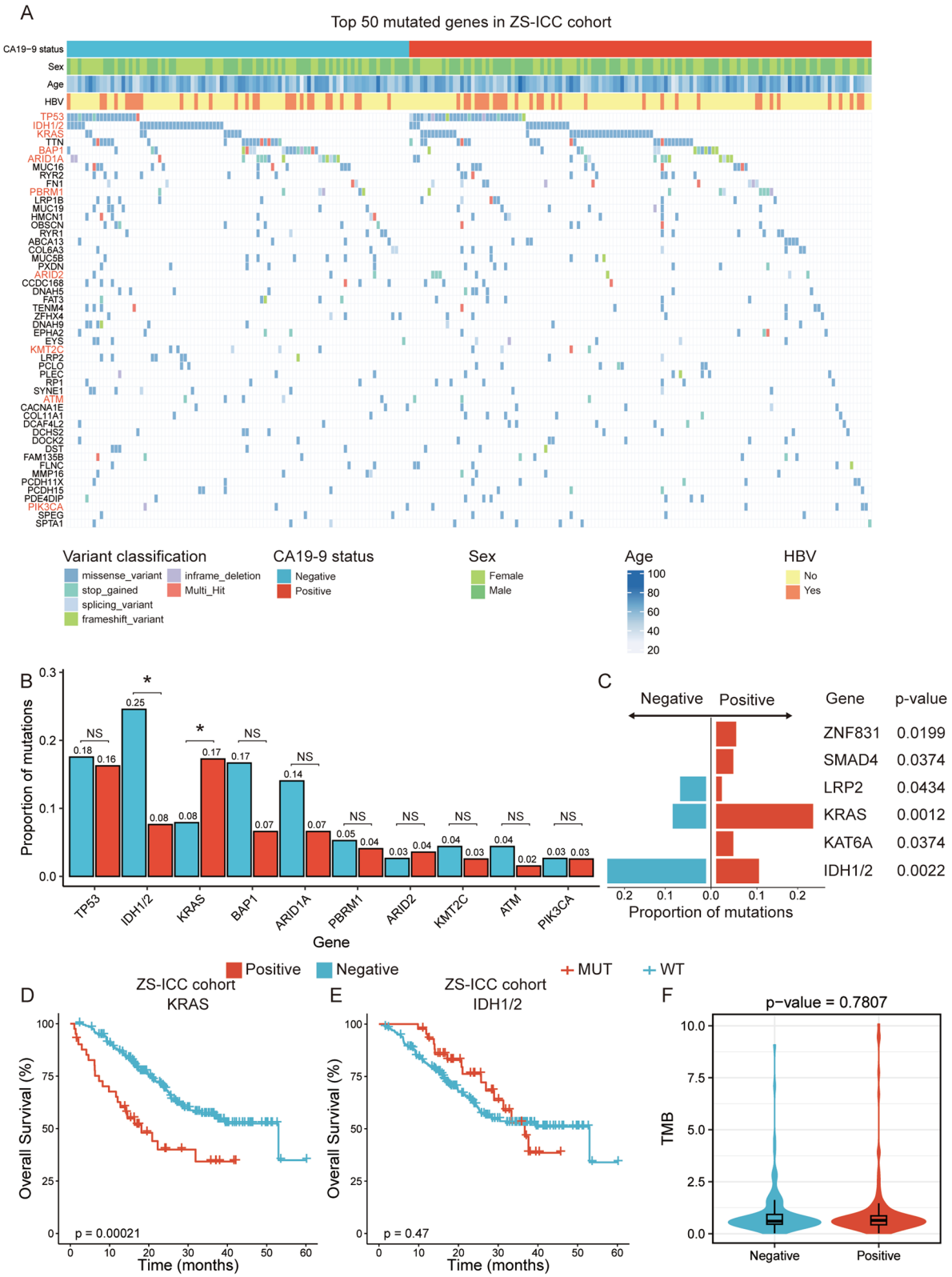

Fig. 2 (See legend on previous page.)

we divided the spots into two main clusters and classified them as tumor and pera-tumor regions based on the expression patterns of KRT19 and ALB (Fig. 5E). We separately assessed the infiltration scores of three glycolysis-related cell subclusters within the tumor region spots. The result revealed a pattern of co-localization for these subclusters within the tumor area (Fig. 5F). Furthermore, by analyzing the correlation of cell scores in each spot, we observed significant positive correlations among these cell subclusters (Fig. 5G). This finding suggests that these subclusters may be co-recruited within the tumor microenvironment and form an interactive cellular network. To further validate the association of these cellular communities with tumor progression, we constructed a GRCC signature by combining the top 50 genes from each of the three cell subclusters. In the ZS-ICC cohort, we found that the GRCC signature score was higher in CA19-9 positive patients and was significantly correlated with poorer prognosis. Additionally, the GRCC score showed a significant positive correlation with glycolysis pathway scores and serum CA19-9 levels (Fig. 5H). In multivariate COX regression analysis, a high GRCC signature score was identified as an independent risk factor affecting OS (Fig. 5I). Encouragingly, we observed broadly consistent results in both the TCGA-ICC cohort and the GSE179423-ICC cohort, indicating that our findings are reproducible and generalizable (Supplementary Fig. 7A, B). In groups with high GRCC signature scores, the incidence of aggressive phenotypes such as intrahepatic metastasis, neural invasion, vascular invasion, lymph node metastasis, and distal metastasis was also higher (Supplementary Fig. 7C), further emphasizing the close link between these glycolytic cellular communities and tumor aggressiveness. Finally, in five independent cohorts, we confirmed that the GRCC signature score in the tumor area was significantly higher than in the peritumoral area (Supplementary Fig. 7D). In summary, our results reveal that CA19-9 positive ICC patients tend to form a greater abundance of glycolysis-related cellular communities, which may lead to a more aggressive tumor phenotype and a poorer prognosis.

Hypoxia induces the formation of glycolysis-related cellular communities by promoting metabolic reprogramming

To investigate the origin and developmental trajectories of these three glycolytic-related cell clusters, we constructed evolutionary trajectories in each major cell type using the Monocle2 algorithm. In the epithelial cells, we identified five different cell states that form two distinct evolutionary branches (Lineage1 and Lineage2, Supplementary Fig. 8A). Similarly, we identified five and seven cellular states in the stromal cells and macrophages, forming three evolutionary branches (Lineage1, Lineage2, and Lineage3, Supplementary Fig. 8B, C). We observed that the three glycolysis-related cell clusters were mainly located at the end of the pseudotime trajectory. To further clarify the specific branches of these three clusters during evolution, we assessed the proportionate changes of each subcluster across different states. In epithelial cells, the Epi_SLC2A1 showed an increasing trend across both Lineage1 and Lineage2 branches (Supplementary Fig. 8D). In stromal cells, the CAF_VEGFA exhibited an increasing trend only in Lineage3, while in macrophages, the Mph_SPP1 showed an increasing trend solely in Lineage2 (Supplementary Fig. 8E, F). These results suggest that all two branches of epithelial cells represent the evolutionary trajectories of Epi_SLC2A1, while CAF_VEGFA and Mph_SPP1 need to follow specific evolutionary branches in their major cell types. We further assessed the hallmark pathways along their evolutionary trajectories. As expected, the glycolysis pathway was significantly enriched in the terminal states of all trajectories (Supplementary Fig. 9A-C). Concurrently, the oxidative phosphorylation (OXPHOS) pathway was more prevalent in the initial states, indicating a metabolic shift from OXPHOS to glycolysis—a common feature across these three cellular evolutionary trajectories. In trajectory plots, we distinctly tracked a decreasing trend in OXPHOS pathway scores and an increasing trend in glycolytic pathway scores along the trajectories, exhibiting a markedly opposite trend (Fig. 6A–C). Correlation analysis further confirmed significant associations

(See figure on next page.)

Fig. 3 The analysis of the transcriptome and proteome between CA19-9 positive and negative patients. **A**–**C** The volcano plots show the significantly differentially expressed genes (logFC > 0.5 & P < 0.05) between CA19-9 positive and negative groups in ZS-ICC (**A**), TCGA-ICC (**B**) and GSE107943-ICC (**C**) cohorts. **D**–**F** The bar plots show the differences of GSEA on hallmark pathways between CA19-9 positive and negative groups in ZS-ICC (**D**), TCGA-ICC (**E**), and GSE107943-ICC (**F**) cohorts. **G** The Venn diagram shows upregulated hallmark pathways overlapping across different ICC cohorts. **H**–**J** The KM curves show that patients in the CA19-9 positive group exhibit poorer OS in ZS-ICC (**H**), TCGA-ICC (**I**), and GSE107943-ICC (**J**) cohorts. **K**–**M** The scatter plots show the correlation between the serum CA19-9 levels and hypoxia glycolysis scores in ZS-ICC (**K**), TCGA-ICC (**L**) and GSE107943-ICC (**M**) cohorts. **N** The volcano plots show the significantly differentially expressed proteins (logFC > 0.5 & P < 0.05) between CA19-9 positive and negative groups in the ZS-ICC cohort. **O** The bubble plot shows the enrichment results on glycolysis-related pathways of the upregulated proteins (logFC > 0 & P < 0.05) in the ZS-ICC cohort. P-values were calculated using the Log-rank test in (**H**–**J**) and the Spearman correlation test in (**K**–**M**)

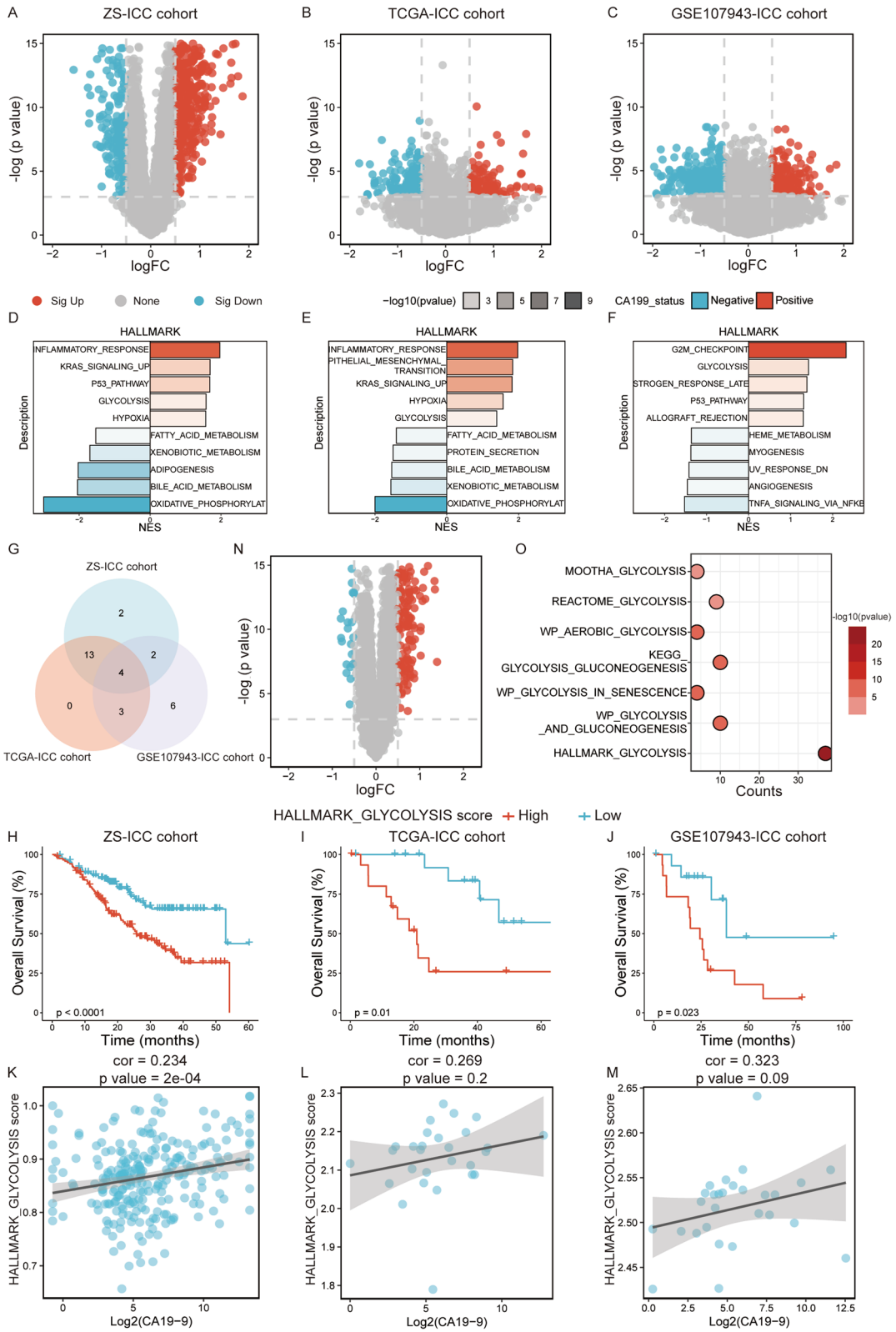

Fig. 3 (See legend on previous page.)

between pseudotime and the signature scores of these metabolic pathways, particularly pronounced in the CA19-9 positive group (Fig. 6D–F). In GSEA conducted across three cohorts, we similarly observed opposing activation patterns between the OXPHOS and glycolysis pathways (Supplementary Fig. 8G). Integrating the above findings, our study reveals that these three glycolysis-related cell clusters may have evolved through metabolic reprogramming.

ICC is characterized by its scarcity of blood vessels, which frequently results in hypoxic conditions within the tumor microenvironment. In the previous section, we observed an increasing trend of hypoxia signature in all three trajectories (Supplementary Fig. 9A-C). Given the close relationship between OXPHOS and glycolysis pathways with hypoxia, we hypothesized that hypoxia might be a potential factor driving metabolic shifts and ultimately promoting the formation of glycolysis-related cell clusters. To prove this hypothesis, we performed a correlation analysis between hypoxia pathway scores and pseudotime, showing a positive correlation with three glycolysis-related cellular evolutionary trajectories (Fig. 6G). Furthermore, the sample's hypoxia score was positively correlated with the proportions of Epi_SLC2A1, CAF_VEGFA, and Mph_SPP1 (Fig. 6H). Notably, samples with higher hypoxia scores were more common in the CA19-9 positive group, although this difference did not reach statistical significance due to the limited sample size (Supplementary Fig. 8H). In the ZS-ICC cohort, we also observed a positive correlation between hypoxia, glycolysis, and GRCC scores, and a negative correlation with OXPHOS scores (Supplementary Fig. 8I-K). Additionally, we performed IHC staining for the hypoxia marker HIF1a on tissue samples from 54 ICC patients. The results indicate that the CA19-9 positive group exhibits a higher fraction of HIF1a staining, and the difference was statistically significant (Fig. 6I, J). With increased HIF1a staining fraction, Epi_SLC2A1, CAF_VEGFA, and Mph_SPP1 were also increased (Supplementary Fig. 10A, B). Collectively, we observed a more hypoxic tumor microenvironment in CA19-9 positive ICC patients, which triggered more active metabolic reprogramming, leading to an increased accumulation of glycolysis-related cell communities.

Deciphering the cellular interaction network among glycolysis-related cellular communities

To further explore the interactions between glycolysis-related cell clusters, we used the NicheNet algorithm to analyze the ligand-receptor (LR) interaction networks between these cells. Intriguingly, the enrichment analysis on the predicted targeted genes of the three cell clusters all showed significant enrichment in oxygen level responses and glycolysis (Fig. 6L, Supplementary Fig. 11B, D). This discovery suggests that the interactions between the three clusters play an essential role in their development and functional maintenance. In the LR interaction between CAF_VEGFA and Mph_SPP1 and Epi_SLC2A1, we found several molecules among the high activity ranking ligands with crucial roles in cell proliferation and migration, such as TGFB1, CXCL12, FGF11, and GDF15 (Fig. 6K). Additionally, the enrichment analysis on the predicted targeted genes of Epi_SLC2A1 focused on biological processes like epithelial cell migration, cell growth, and cell adhesion (Fig. 6L), indicating that the other two cell clusters may regulate the EMT of Epi_SLC2A1. Further analysis showed that Epi_SLC2A1 has a marked upregulation of the EMT pathway and a higher EMT score compared to other epithelial cells (Fig. 7A, B), and the EMT score of epithelial cells is also highest at the end of the evolutionary trajectories, and is positively correlating with pseudotime (Fig. 7C). Using the CellChat analysis, we observed an increase in the number and intensity of communication between the three glycolysis-related cell types in CA19-9 positive

(See figure on next page.)

Fig. 4 Single-cell analysis for all cells and epithelial cells. **A** The UMAP plot shows all cells colored by major cell types. **B** The dot plot shows the expression of the canonical marker genes across the eight major cell types. **C** The bar plot shows the numbers of each major cell type. **D** The UMAP feature plot shows the hallmark glycolysis scores in all cells. **E** The violin plot shows the difference in hallmark glycolysis scores in eight major cell types. **F** The heatmap shows eight major cell types' interaction number differences between CA19-9 positive and negative groups. **G** The UMAP plot shows epithelial cells colored by seven epithelial subclusters. **H** The dot plot shows the expression of the marker genes across the seven epithelial subclusters. **I**, **J** The bar plot (**I**) and heatmap (**J**) show the proportion differences and Ro/e values of seven epithelial subclusters between CA19-9 positive and negative groups. *: Ro/e > 1. **K** The UMAP feature plots show the hallmark glycolysis scores (left) and glycolysis/gluconeogenesis scores (right) in epithelial cells. **L** The violin plots compare hallmark glycolysis scores (left) and glycolysis/gluconeogenesis scores (right) between Epi_SLC2A1 and other epithelial cells. **M** The GSEA result of hallmark glycolysis pathway between Epi_SLC2A1 and other epithelial cells. **N** The dot plot shows the expression of the LDHA, HK2, and PKM across the seven epithelial subclusters. **O** The violin plot shows the differences in GRCC scores between the CA19-9 positive and negative groups in the ZS-ICC cohort (up left panel). The KM curves compare the high and low GRCC score groups on OS in the ZS-ICC cohort (upright panel). The scatter plots show the correlation between GRCC scores, hallmark glycolysis scores (bottom left panel), and serum CA19-9 levels (bottom left panel) in the ZS-ICC cohort. P-values were calculated using the Student's t-test in (**L**) and (**O**) (up left panel), the Log-rank test in (**O**) (upright panel), and the Spearman correlation test in (**O**) (bottom panel)

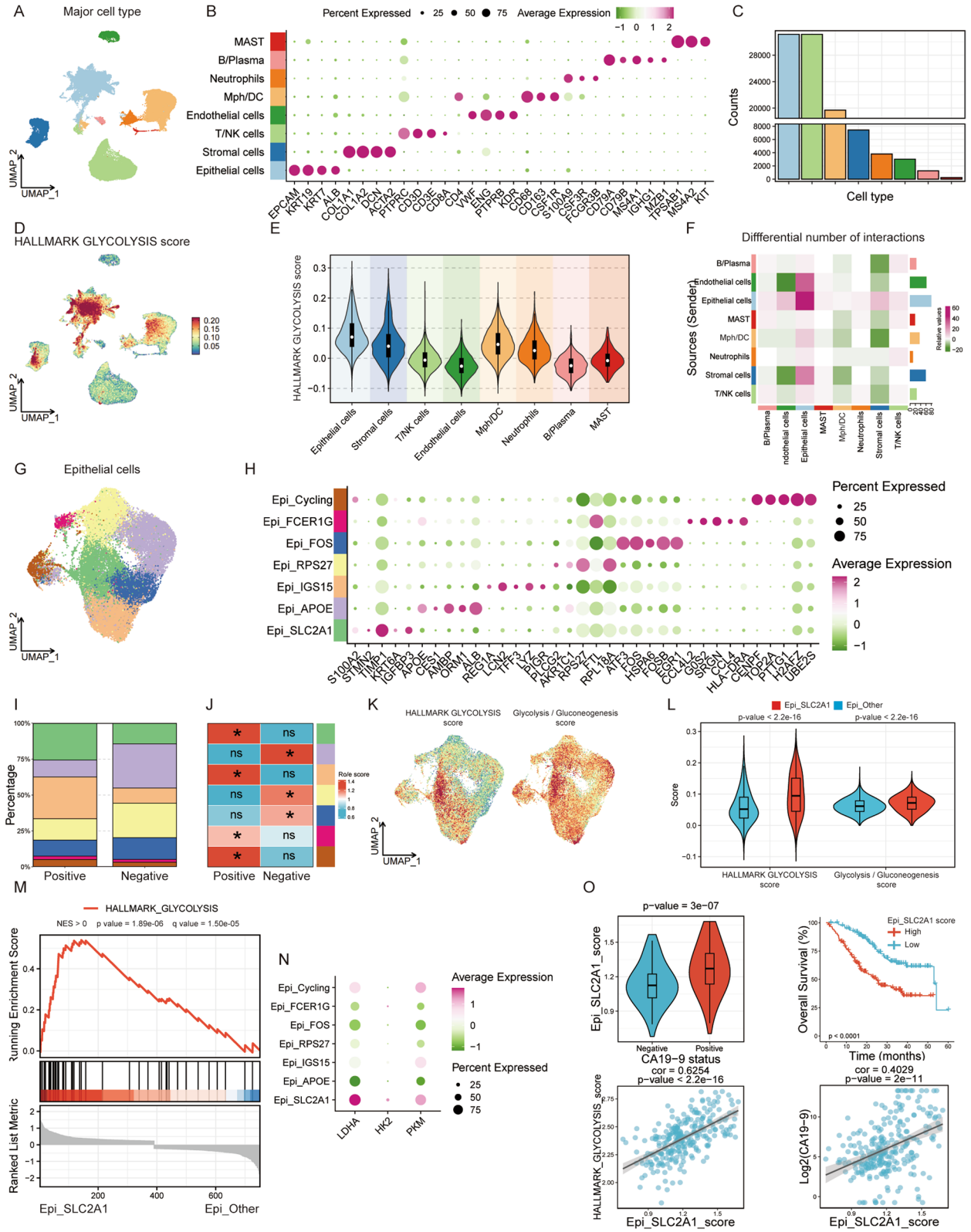

Fig. 4 (See legend on previous page.)

ICC, and signaling pathways closely associated with EMT, such as the TGFb, ncWNT, and EGF pathways, exhibited significant upregulation (Fig. 7D, Supplementary Fig. 12A, B). Notably, when using Epi_SLC2A1 as the receptor, the TGFB1 ligand signal was significantly enhanced in the three cell types of the CA19-9 positive group (Fig. 7E). In addition, the activity of TGFB1 also ranks high in LR interaction analysis with CAF_VEGFA and Mph-SPP1 (Supplementary Fig. 11A, C), indicating that TGFB1 plays a crucial role in regulating the interaction network between glycolysis-related cell clusters. For CAF_VEGFA, the predicted targeted genes were mainly enriched in tissue remodeling, cell–matrix adhesion, and mesenchymal cell differentiation (Supplementary Fig. 11B), essential for tumor metastasis [49–51]. For Mph_SPP1, the enriched terms were related to lipid transport, lipid storage, and myeloid cell activation (Supplementary Fig. 11D), which have been implicated in M2 polarization of macrophages in previous studies [52–54]. In summary, our findings indicate that the crosstalk among the three glycolysis-related cell clusters constitutes a vicious cycle that promotes their own formation and maintenance plays a crucial role in tumor metastasis and invasion.

Glycolysis-related cellular communities promote tumor angiogenesis

The enrichment analysis on the predicted target genes of the three glycolysis-related cell clusters all showed positive regulation on vascular development (Fig. 6L, Supplementary Fig. 11B, D), suggesting that these cells may have the function of promoting tumor angiogenesis. VEGFA, a factor crucial for angiogenesis, activates endothelial cell proliferation by binding to its receptors on the surface of endothelial cells. In our data, we noted generally higher expression levels of VEGFA in these glycolysis-related cell clusters (Fig. 7F). In the ZS-ICC cohort, samples with high GRCC scores exhibited higher VEGFA expression, with a significant positive correlation between the two (Supplementary Fig. 12C). Moreover, CellChat analysis demonstrated a significant increase in VEGFA ligand signing between these three glycolysis-related cells and endothelial cells compared to other cells (Supplementary Fig. 12D). As expected, the communication probability between these three cell clusters and endothelial cells showed a general increase in the CA19-9 positive ICC patients (Fig. 7G). Subsequently, we subclassified endothelial cells into seven distinct subclusters (Fig. 6H, Supplementary Fig. 11E, F, Supplementary Table 13). We found that the EC_Tip_ESM1 had the closest interactions in VEGFA signing with the three glycolysis-related cells (Fig. 6I), suggesting it may be the critical subcluster influenced by these cells. In three independent cohorts, the top 50 signature score of the EC_Tip_ESM1 showed a positive correlation with GRCC scores, and KM analysis also indicated that the higher End_Tip_ESM1 score group tended to have poorer OS (Supplementary Fig. 11G, H). In summary, we found that high expression levels of VEGFA often accompany glycolysis-related cell clusters. VEGFA promotes endothelial cell proliferation and angiogenesis by activating receptors on endothelial cells. This process provides more blood supply to the tumor, which may enhance its invasiveness and metastatic potential of the tumor.

Therapeutic drug screening for GRCC and CA19-9 positive ICC patients

This study employed a two-stage strategy to screen therapeutic drugs for GRCC and CA19-9 positive ICC patients (Fig. 7I). Through this method, we identified 28 CTRP-derived drugs targeting GRCC and 12 drugs specifically suitable for CA19-9 positive ICC patients. After intersection analysis, we selected six drugs that yielded significantly lower AUC values in GRCC and CA19-9 positive ICC patients and showed negative correlations with the GRCC scores (Supplementary Fig. 13A–F). Among these

(See figure on next page.)

Fig. 5 Glycolysis-related cell subclusters were verified using mIF and spatial transcriptomics analysis. **A**–**C** The representative mIF images of Epi_SLC2A1 (**A**, blue: DAPI, green: GLUT1, red: CK19), CAF_VEGFA (**B**, blue: DAPI, green: VEGFA, red: αSMA), and Mph_SPP1 (**C**, blue: DAPI, green: SPP1, red: CD68) in CA19-9 positive (bottom panel) and negative (up panel) groups. Scale bar = 50um. **D** The box plots show the differences in counts/unit area in Epi_SLC2A1 (left panel), CAF_VEGFA (mid panel), and Mph_SPP1 (right panel) between CA19-9 positive and negative groups (positive: n = 14, negative: n = 12). **E** The UMAP (up left panel) and spatial (up right panel) plots show all spots colored by tissue types. The spatial feature plots show the expression of KRT19 (bottom left panel) and ALB in all spots (bottom left panel). **F** The spatial feature plots show the Epi_SLC2A1 (left panel panel), CAF_VEGFA (mid panel panel), and Mph_SPP1 (right panel panel) signature scores in tumor region spots. **G** The correlation analysis between the Epi_SLC2A1 and CAF_VEGFA signature scores, between the Epi_SLC2A1 and Mph_SPP1 signature scores, and between the CAF_VEGFA and Mph_SPP1 signature scores in tumor region spots. **H** The violin plots show that the CA19-9 positive group has higher GRCC scores in the ZS-ICC cohort (up left panel). The KM curves show that the high GRCC scores group has a poorer OS in ZS-ICC cohorts (upright panel). The scatter plots show that the GRCC scores significantly correlate with hallmark glycolysis scores (bottom left panel) and serum CA19-9 levels (bottom right panel) in the ZS-ICC cohort. **I** The forest plot shows the multivariate Cox regression result for OS in the ZS-ICC cohort. P-values were calculated using the Mann-Whitney U test in (**D**), the Pearson correlation test in (**G**), the Student's t-test in (**H**) (up left panel), the Log-rank test in (**H**) (upright panel), and the Spearman correlation test in (**H**) (bottom panel).

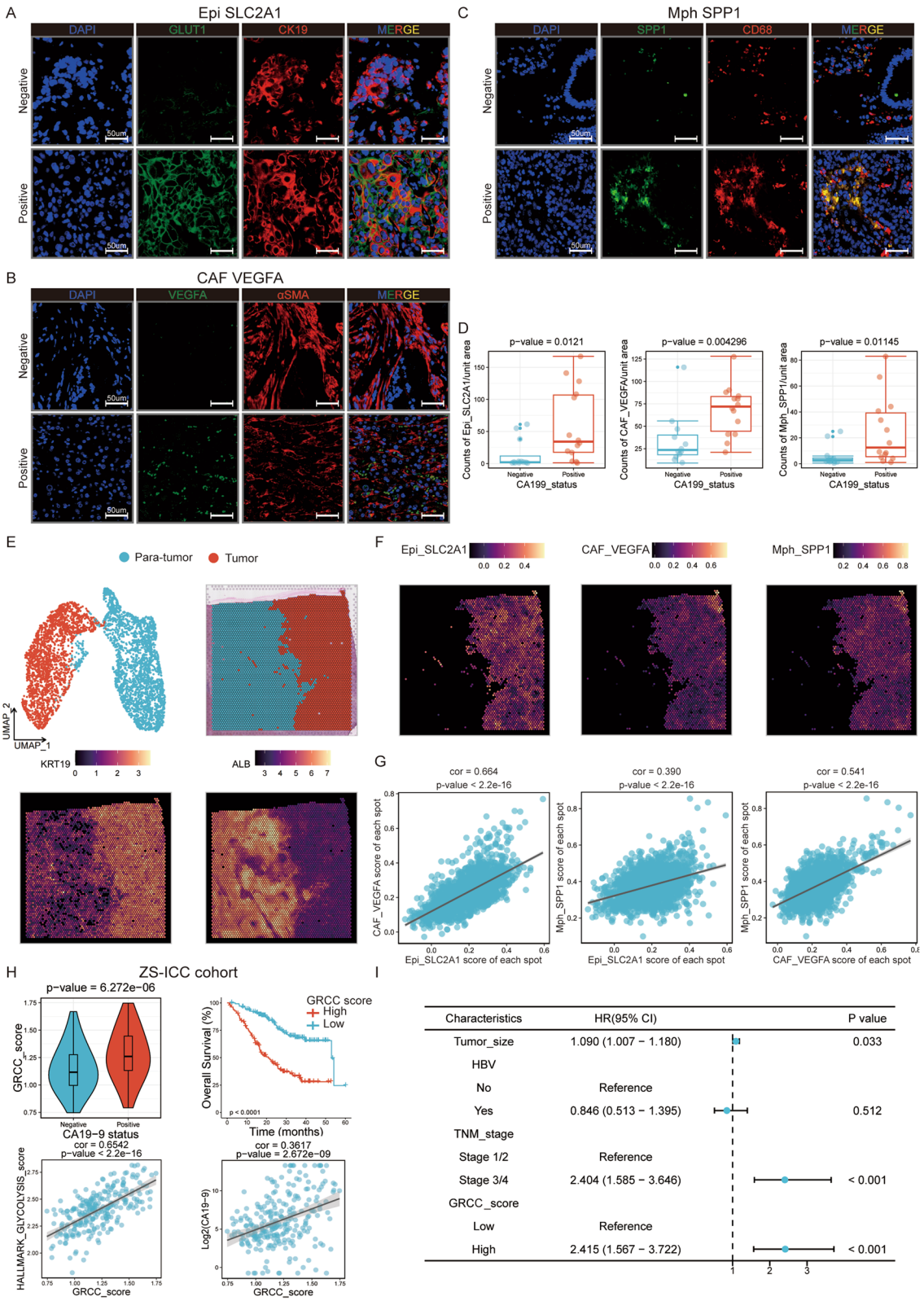

Fig. 5 (See legend on previous page.)

candidate drugs, Selumetinib and Trametinib were the main components, with the remaining four drugs being combined applications of these two agents. By querying the CTRP database, we discovered that both are MEK inhibitors. As a pivotal regulatory factor in the MAPK signaling pathway, MEK plays a crucial role in controlling essential biological processes such as cell proliferation, differentiation, migration, and survival. Interestingly, we observed a significant enrichment of the MAPK signaling pathway in the enrichment analysis on the predicted target genes of Epi_SLC2A1 (Fig. 6L). This result further corroborates the potential application value of these candidate drugs.

Discussion

In recent years, the continuous updating of ICC diagnostic and treatment methods has led to improved standards and concepts. However, due to the lack of early symptoms, patients are often diagnosed at an advanced stage with a poor prognosis. This is especially true for CA19-9 positive ICC patients, whose tumors are more invasive and metastatic, significantly affecting long-term survival. Studies have shown that ICC patients with persistently elevated CA19-9 levels are more likely to develop tumor recurrence and metastasis [55]. A study by Asaoka et al. showed that the 5-year OS of ICC patients with normal and elevated CA19-9 was 79.9% and 38.7%, respectively, indicating a poorer prognosis for CA19-9-positive patients [21]. Our results showed that CA19-9-positive ICC patients were likelier to have perineural invasion, vascular invasion, lymph node metastasis, and distant metastasis. Their OS and RFS were significantly lower than those of CA19-9-negative patients, confirming CA19-9 as an essential marker for the aggressive phenotype and poor prognosis of ICC. This study integrated multi-omics data to systematically elucidate the aggressive mechanisms and potential therapeutic strategies for CA19-9-positive ICC. We observed an increased frequency of KRAS mutations, significant upregulation of glycolytic pathways, and, for the first time, characterized the role of specific cell subpopulations in the tumor microenvironment. Compared to previous studies, our research provides a novel elucidation of the association between the tumor microenvironment and metabolic reprogramming, offering a clinical basis for individualized therapeutic strategies. These findings suggest new avenues for developing targeted therapies against specific cell populations with significant potential for clinical application.

Investigating the molecular mechanisms underlying prognostic differences in ICC patients revealed a significant association between serum CA19-9 levels and the aberrant expression of related driver genes. Genomically, KRAS mutations were more common in CA19-9-positive ICC patients than CA19-9-negative patients, potentially explaining their increased invasiveness and metastasis. The KRAS proto-oncogene encodes an oncogenic protein involved in tumor growth and metastasis. It is a member of the GTPase family involved in various adenocarcinomas, including ICC, through critical signaling pathways [56–58]. A large cohort study of 1024 ICC patients by Zhou et al. reported a KRAS mutation rate of 12.4% and detailed the distribution of KRAS variant subtypes [59]. However, their study did not explore the correlation between CA19-9 expression levels and KRAS mutations. Our study also showed that KRAS mutations were frequent in CA19-9 positive ICC patients and were associated with increased aggressiveness and poorer OS and RFS. In contrast, IDH1/2 mutations were more prevalent in the CA19-9 negative group. These findings suggest significant differences in the distribution of crucial driver genes between CA19-9-positive and negative ICC patients, potentially underlying the molecular basis for their differing clinical prognoses. Our findings further emphasize the need to understand the mechanisms of driver genes like KRAS in ICC for developing more effective individualized therapies, filling gaps in previous research.

The glycolytic pathway, a critical metabolic feature, is upregulated in CA19-9-positive ICC and is closely related

(See figure on next page.)

Fig. 6 The analysis of evolutionary trajectories and cellular interaction network. **A-C**. Trajectory plots of epithelial cells (**A**), stromal cells (**B**), and macrophages (**C**) colored by hallmark OXPHOS (left panel) and glycolysis (right panel) scores. **D**–**F** The correlation analysis between pseudotime and hallmark OXPHOS (left panel) and glycolysis (right panel) scores in epithelial cells (**D**), lineage 3 of stromal cells (**E**), and lineage 2 of macrophages (**F**). **G** The correlation analysis between pseudotime and hallmark hypoxia scores in epithelial cells (left panel), lineage 3 of stromal cells (mid panel), and lineage 2 of macrophages (right panel). **H** The scatter plots show the correlation between the hallmark hypoxia scores of each sample and the proportion of Epi_SLC2A1 (left panel), CAF_VEGFA (mid panel), and Mph_SPP1 (right panel). **I** The representative IHC images of the HIF1αstaining in CA19-9 positive (up panel) and negative group (bottom panel). Scale bar = 100um. **J** The box plot shows the differences in the fraction of HIF1αstaining between CA19-9 positive and negative groups (positive: n = 31, negative: n = 22). **K** The heatmaps of Nichenet analysis show regulatory patterns between CAF_VEGFA to Epi_SLC2A1 (up panel) and Mph_ SPP1 to Epi_SLC2A1 (bottom panel). **L** The bar plots show the GO and KEGG pathways enrichment results of the predicted target genes in Epi_SLC2A1. P-values were calculated using the Student's t-test in (**J**) and the Spearman correlation test in (**D**–**H**)

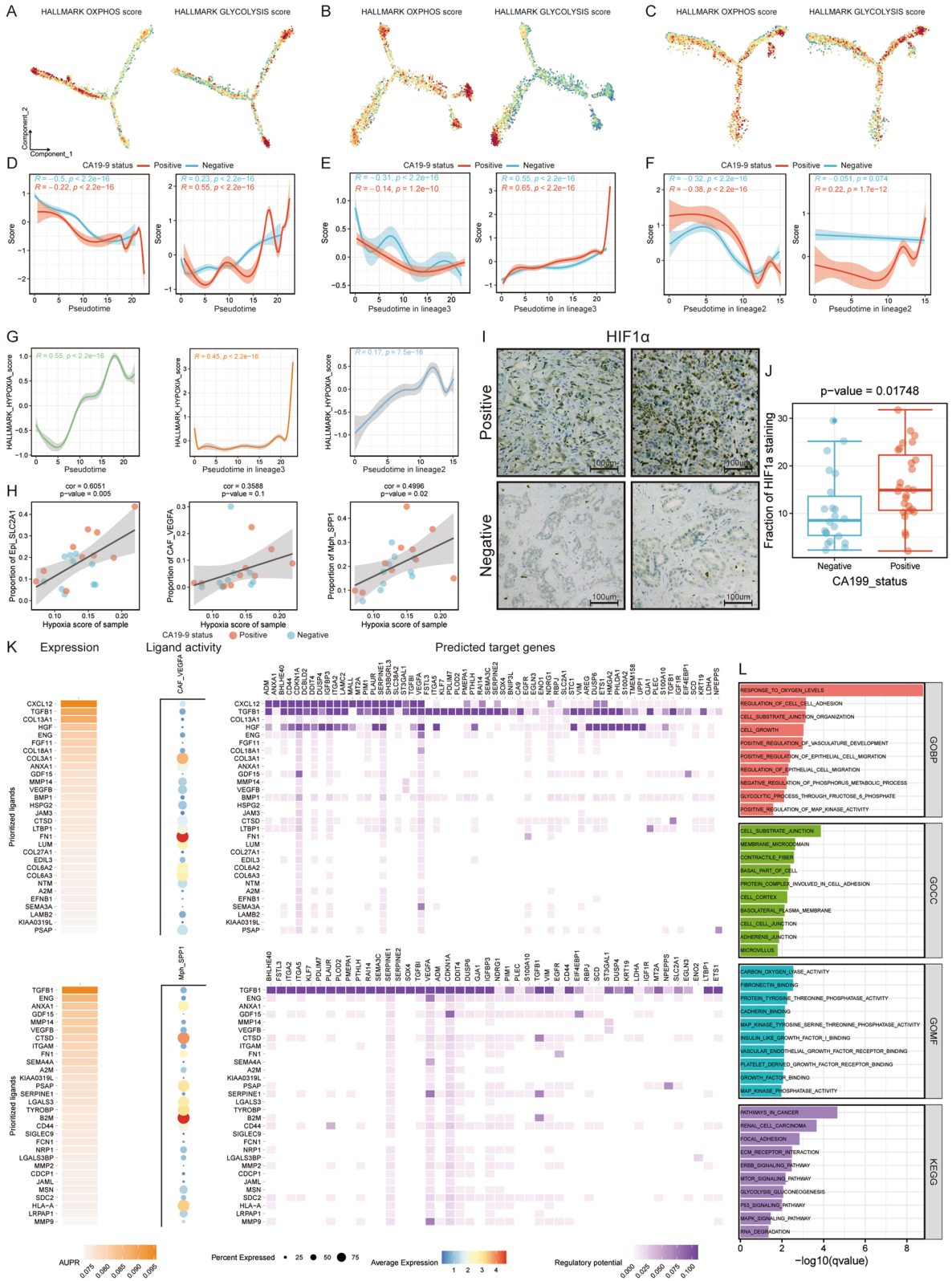

Fig. 6 (See legend on previous page.)

to tumor cell behavior and patient prognosis. This study showed that the glycolytic pathway was significantly upregulated in CA19-9-positive ICC while the OXPHOS pathway decreased. Additionally, we found that activation of the glycolytic pathway was closely associated with KRAS mutations, which were significantly more frequent in CA19-9-positive patients. These patients also had higher glycolysis scores, suggesting that KRAS mutations may drive tumor aggressiveness by promoting glycolysis. Bartman et al. demonstrated that KRAS mutations are strongly associated with the activation of glycolysis in tumor cells by activating glycolysis and inhibiting the tricarboxylic acid cycle (TCA cycle), causing tumor cells to rely primarily on glycolysis for ATP production [60]. Despite the increased rate of glycolysis, its ATP production is insufficient to fully compensate for the reduced ATP from the TCA cycle, resulting in a low rate of total ATP synthesis. To adapt to the low energy supply, tumor cells reduce energy-intensive functions, such as protein synthesis, to maintain rapid proliferation, thereby gaining a growth advantage under energy-limited conditions. This mechanism explains the metabolic characteristics of KRAS mutant tumors and their growth advantage under energy-limited conditions, echoing the results of the present study.

The synergistic effect of KRAS mutation and HIF-1α in ICC cells is crucial in regulating the glycolytic pathway and enhancing invasive and metastatic potential. KRAS mutations upregulate essential glycolytic genes such as GLUT1, HK2, and LDHA by activating the MAPK/ERK and PI3K/AKT pathways. This enhances glucose uptake and metabolite accumulation to meet the energy demands of rapid tumor proliferation, promoting ICC cell growth and survival [61, 62]. Under hypoxic conditions, HIF-1α is activated, further enhancing tumor metabolic activity by upregulating glycolytic enzymes and promoting lactate accumulation [63, 64]. Lactate accumulation alters the acid–base balance in the tumor microenvironment, leading to overexpression of matrix-degrading enzymes (e.g., MMPs), enhancing invasive and metastatic potential while suppressing anti-tumor immune responses and promoting tumor spread [65, 66]. Our study found higher HIF-1α expression in the CA19-9-positive group, further supporting its critical role in the hyperglycolytic state. Targeting HIF-1α or blocking its downstream glycolytic enzymes (e.g., HK2 and LDHA) has been proposed as an effective strategy to weaken tumor adaptation in hypoxic environments. This provides a theoretical basis for targeting KRAS and HIF-1α in ICC therapy.

The TME of ICC is a highly complex and dynamic system characterized by a rich fibrous stroma and high reactivity that exhibits immunosuppressive and pro-tumorigenic functions [67, 68]. CA19-9-positive ICC patients exhibit higher levels of glycolytic activity because tumor cells promote glucose metabolism reprogramming by upregulating key enzymes such as hexokinase 2 (HK2), pyruvate kinase M2 (PKM2), and lactate dehydrogenase A (LDHA) [69, 70]. This metabolic reprogramming meets the demand for energy and biosynthetic precursors for rapid tumor cell growth and division but also alters the tumor microenvironment by regulating lactate production and efflux, further promoting tumor aggressiveness and resistance to therapy [71]. Additionally, glycolysis is closely related to tumor progression processes such as immune escape, angiogenesis, and EMT [72, 73]. Building on this, using single-cell RNA sequencing, our study revealed high heterogeneity in CA19-9-positive ICC patients. We identified specific cellular subclusters enriched with glycolytic features, including Epi_SLC2A1, CAF_VEGFA, and Mph_SPP1, all strongly associated with poor ICC prognosis. Spatial transcriptome analysis indicated that these cell subclusters play a crucial role in forming a highly invasive TME through forming highly interactive cellular communities.

(See figure on next page.)

Fig. 7 The effects of glycolysis-related cellular communities on EMT, angiogenesis, and drug screening strategy. **A** The GSEA result of hallmark EMT pathway between Epi_SLC2A1 and other epithelial cells. **B** The UMAP feature (up panel) and violin (bottom panel) plots show the Epi_SLC2A1 has higher hallmark EMT scores compared to other epithelial cells. **C** The trajectory plot (up panel) shows the hallmark EMT scores and the correlation analysis (bottom panel) between pseudotime and hallmark EMT scores in epithelial cells. **D** The circle plots show the differences in the number (up panel) and intensity (bottom panel) of interactions within the three glycolysis-related cell subclusters between CA19-9 positive and negative groups. Red represents increasing, and blue represents decreasing in the positive group. **E** The dot plot shows the differences in TGFB1 signaling interaction of three glycolysis-related cell subclusters to Epi_SLC2A1 between CA19-9 positive and negative groups. **F** The dot plots show the expression of the VEGFA across the subclusters of stromal cells (left panel), epithelial cells (mid panel), and macrophages (right panel). **G** The dot plot shows the differences in VEGFA signaling interaction of three glycolysis-related cell types to endothelial cells between CA19-9 positive and negative groups. **H** The UMAP plot shows endothelial cells colored by seven endothelial subclusters. **I** The dot plot shows the differences in VEGFA signaling interaction between the three glycolysis-related cell subclusters and seven endothelial subclusters between CA19-9 positive and negative groups. **J** The overall workflow for screening candidate drugs targeting GRCC and CA19-9 positive ICC patients. P-values were calculated using the Student's t-test in (**B**) (bottom panel) and the Pearson correlation test in **C** (bottom panel)

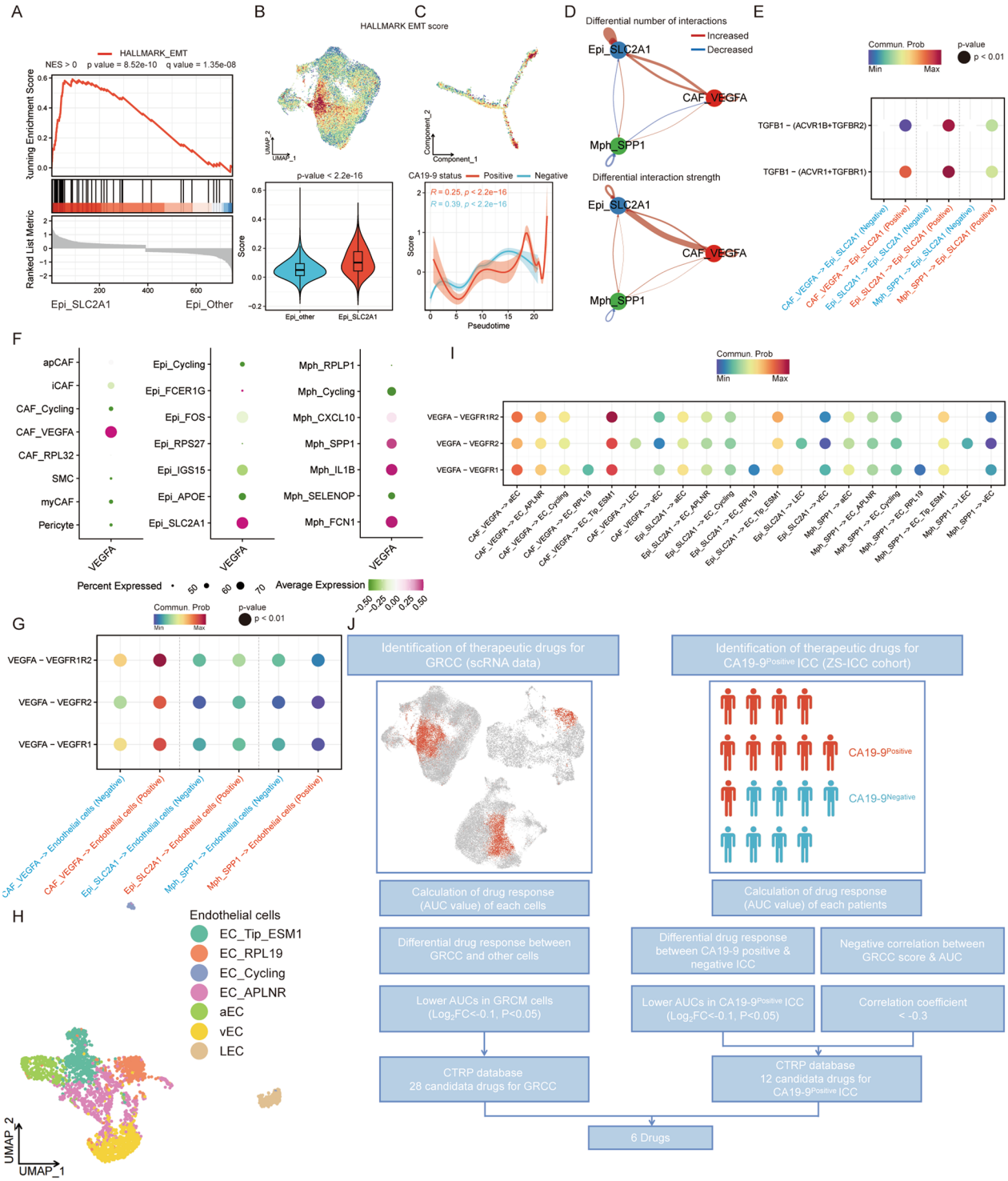

Fig. 7 (See legend on previous page.)

Enhanced communication of TGFβ and Wnt signaling pathways between these cell types promotes tumor metastasis via EMT facilitates angiogenesis through high VEGFA expression interacting with endothelial cells. Additionally, our study found a more hypoxia environment in CA19-9-positive ICC patients. This condition worsened the prognosis by promoting metabolic switching and accumulating glycolytic cellular communities.

In conjunction with previous literature, hypoxia as a stressor can cause tumor cells to acquire a more aggressive phenotype by altering the expression of relevant genes such as HIF1A and VEGFA. This includes genomic instability, autophagy, metabolic remodeling, angiogenesis, migration, infiltration, extracellular matrix remodeling, EMT, stem cell maintenance, immune evasion, and treatment resistance [74]. In response to hypoxic stress, intercellular communication becomes more frequent and complex, increasing the tumor's ability to invade, proliferate, and resist apoptosis, thereby promoting local and distant metastasis and resistance to therapy [75, 76].

ICC, a highly malignant tumor with a poor prognosis, has had limited success with conventional treatments. In recent years, the development of targeted therapy and immunotherapy based on molecular typing has provided new hope for treating such tumors, either alone or in combination with other therapeutic modalities, and progress continues to be made. However, due to the high heterogeneity among patients, there are individual differences in efficacy, and only a tiny proportion of patients achieve lasting benefits [77]. This study identified multiple potential therapeutic targets and drug candidates through drug sensitivity analysis based on multi-omics data, mainly including Selumetinib and Trametinib, which are MEK inhibitors. Gao et al. found that high p-ERK expression was closely associated with advanced tumor TNM stage, increased lymphovascular invasion, and poorer survival. AZD6244 (Selumetinib) regulated VEGF via the p-ERK-c-Fos-HIF-1α integrative signaling pathway, inhibited the MAPK-ERK kinase signaling pathway, thereby blocking angiogenesis and significantly inhibited tumor growth [78]. Morelli et al. demonstrated that combining the MEK inhibitor Selumetinib and the HDAC inhibitor Vorinostat had synergistic antiproliferative activity against KRAS-mutant tumor cell lines. This combination significantly inhibited cell proliferation and sphere formation, promoted apoptosis and G1-phase cell-cycle arrest, and reduced cell migration and VEGF-A secretion [79]. Additionally, a phase II multicenter clinical trial showed that the combination of Trametinib and Dabrafenib had better therapeutic prospects for patients with biliary tract cancer carrying the BRAFV600E mutation [80]. These studies are consistent with the present study's results and explain the possible mechanisms. Taken together, targeted therapeutic strategies based on multi-omics data provide a new pathway for individualized treatment of ICC. Further study of these potential targets and drug combinations will help improve therapeutic efficacy.

This study represents the first systematic integration of multiple omics data to thoroughly explore the mechanisms behind poor prognosis in CA19-9 positive ICC patients. Through comprehensive analysis, we identified specific cell subclusters linked to heightened tumor invasiveness and poor prognosis. Additionally, we uncovered how these subpopulations promote tumor invasiveness and metastasis by forming highly interactive cell communities. Nonetheless, our study has several limitations, including a limited sample size, which restricts the generalizability of our findings. More extensive, multi-center studies are warranted to validate these results more robustly. Additionally, while we utilized multi-omics analysis, specific validation experiments employed relatively simple approaches. Future studies should incorporate multiple technical cross-validation methodologies, enhancing result reliability. Furthermore, although we identified several potential targets, in-depth molecular and functional experiments are essential to delineate their precise roles in cancer progression. Our research provides new insights into the TME and glycolytic activity in ICC and lays a foundation for developing individualized therapeutic strategies targeting these specific cellular subclusters. Future research should focus on expanding sample sizes, leveraging diverse validation techniques, and translating these findings through clinical trials to validate therapeutic efficacy, ultimately bridging the gap between laboratory findings and clinical applications.

Conclusions

This study identified the glycolytic pathway upregulation and hypoxia-driven cellular communities in CA19-9-positive ICC, which are associated with increased invasiveness and poor prognosis. Our findings suggest the potential use of MEK inhibitors as a targeted therapy, contributing to the advancement of personalized treatment strategies in clinical practice. Further clinical validation is necessary to realize the full potential of these therapeutic approaches.

Abbreviations

ICC	Intrahepatic cholangiocarcinoma
CA19-9	Carbohydrate antigen 19-9
WES	Whole-exome sequencing
RNA	Ribonucleic acid
scRNA-seq	Single-cell RNA sequencing
OS	Overall survival
RFS	Recurrence-free survival
KRAS	Kirsten rat sarcoma viral oncogene homolog
IDH1/2	Isocitrate dehydrogenase 1/2
Epi	Epithelial cells
SLC2A1	Solute carrier family 2 member 1
CAF	Cancer-associated fibroblasts
VEGFA	Vascular endothelial growth factor A
Mph	Macrophages
SPP1	Secreted phosphoprotein 1
EMT	Epithelial-mesenchymal transition
CCA	Cholangiocarcinoma
PCC	Perihilar cholangiocarcinoma
DCC	Distal cholangiocarcinoma

HCC	Hepatocellular carcinoma
TME	Tumor microenvironment
GO	Gene ontology
KEGG	Kyoto encyclopedia of genes and genomes
GSEA	Gene set enrichment analysis
NES	Normalized enrichment score
HVGs	Highly variable genes
PCA	Principal component analysis
EPCAM	Epithelial cell adhesion molecule
KRT19	Keratin 19
COL1A1	Collagen type I alpha 1 chain
DCN	Decorin
NK cells	Natural Killer cells
VWF	Von willebrand factor
PECAM1	Platelet and endothelial cell adhesion molecule 1
DC	Dendritic cells
C1QA	Complement C1q A chain
S100A9	S100 calcium binding protein A9
FCGR3B	Fc fragment of IgG receptor IIIb
MS4A1	Membrane spanning 4-domains A1
TPSAB1	Tryptase alpha/beta 1
CNV	Copy number variation
GRCC	Glycolysis-related cellular communities
CCL	Cancer cell lines
CCLE	Cancer cell line encyclopedia
CTRP	Cancer therapeutics response portal
AUC	Area under the curve
IHC	Immunohistochemical
mIF	Multiplexed immunofluorescence
TMA	Tissue microarray
HIF1-α	Hypoxia-inducible factor 1-alpha
HRP	Horseradish peroxidase
CK19	Cytokeratin 19
GLUT1	Glucose transport protein 1
αSMA	Alpha-smooth muscle actin
VEGF	Vascular endothelial growth factor
KM	Kaplan–Meier
TP53	Tumor protein p53
BAP1	BRCA1 associated protein 1
PBRM1	Polybromo 1
TMB	Tumor mutation burden
OXPHOS	Oxidative phosphorylation
LR	Ligand-receptor
TGFb	Transforming growth factor beta
ncWNT	Non-canonical Wnt
EGF	Epidermal growth factor
MAPK	Mitogen-activated protein kinase
TCA cycle	Tricarboxylic acid cycle
HK2	Hexokinase 2
PKM2	Pyruvate kinase M2
LDHA	Lactate dehydrogenase A

Supplementary Information

The online version contains supplementary material available at https://doi.org/10.1186/s12967-024-05854-9.

Supplementary Material 1.

Supplementary Material 2.

Acknowledgements
Thanks to all the authors for their contributions to this manuscript.

Author contributions
D.M., P.W., J.Z., and Z.L. designed the study. D.M., H.L., and Z.L. developed the methodology. D.M., J.H., Z.C., and Y.C. acquired the data. D.M., P.W., and Z.L. analyzed and interpreted the data. P.W., H.L., J.H., Y.C., W.S., and Z.Y. provided technical and material support. Q.C., J.G., and J.Z. supervised the study. D.M., P.W., J.Z., and Z.L. wrote and reviewed the manuscript.

Funding
This work was supported by the Capital Health Research and Development of Special Fund (2022-2-4084) and the Peking University People's Hospital Scientific Research Development Funds (RDX2023-09).

Availability of data and materials
The RNA-seq and chip microarray data used in this study are available in the UCSC Xena portal (https://xenabrowser.net/datapages/) and the Gene Expression Omnibus (https://www.ncbi.nlm.nih.gov/geo/) under accession code GSE107943, GSE76297, GSE32225, and GSE26566. The data of MSK-ICC cohort was download from cBioPortal for Cancer Genomics (https://www.cbioportal.org/study/summary?id=ihch_msk_2021). The data of ZS-ICC cohort was download from biosino NODE database (https://www.biosino.org/node/project/detail/OEP001105). The scRNA-seq data used in this study were deposited in National Genomics Data Center (https://ngdc.cncb.ac.cn/bioproject/browse/PRJCA007744). All other data are in the manuscript, supplementary materials or available from the corresponding author upon reasonable request.

Declarations

Ethics approval and consent to participate
This study was approved by the Peking University People's Hospital Ethics Committee. All procedures involving human participants were performed in accordance with the ethical standards of the institutional and national research committee and with the 1964 Helsinki declaration and its later amendments or comparable ethical standards. Informed consent was obtained from all individual participants included in the study.

Consent for publication
Consent for publication was obtained from all individual participants included in the study.

Competing interests
The authors declare that they have no competing interests.

Author details
[1]Department of Hepatobiliary Surgery, Peking University People's Hospital, Beijing, China. [2]Beijing Key Laboratory of HCC and Liver Cirrhosis, Peking University People's Hospital, Beijing, China. [3]Peking University Center of Liver Cancer Diagnosis and Treatment, Peking University People's Hospital, Beijing, China. [4]Peking University Institute of Organ Transplantation, Peking University People's Hospital, Beijing, China. [5]Peking University-Yunnan Baiyao International Medical Research Center, Beijing 100191, China. [6]Peking University First Hospital, Beijing 100191, China. [7]Department of Hepatobiliary Surgery, Peking University International Hospital, Life Park Road No.1 Life Science Park of Zhong Guancun, Chang Ping District, Beijing 102206, China. [8]Department of General Surgery, Civil Aviation General Hospital, Beijing 100123, China.

Received: 21 July 2024 Accepted: 4 November 2024
Published online: 15 November 2024

References

1. Bray F, Laversanne M, Sung H, Ferlay J, Siegel RL, Soerjomataram I, et al. Global cancer statistics 2022: GLOBOCAN estimates of incidence and mortality worldwide for 36 cancers in 185 countries. CA Cancer J Clin. 2024;74(3):229–63.
2. Ali I, Wani WA, Haque A, Saleem K. Glutamic acid and its derivatives: candidates for rational design of anticancer drugs. Future Med Chem. 2013;5(8):961–78.
3. Ali I, Wani WA, Saleem K, Wesselinova D. Syntheses, DNA binding and anticancer profiles of L-glutamic acid ligand and its copper(II) and ruthenium(III) complexes. Med Chem. 2013;9(1):11–21.
4. Ali I, Wani WA, Saleem K, Hsieh M-F. Anticancer metallodrugs of glutamic acid sulphonamides: in silico, DNA binding, hemolysis and anticancer studies. RSC Adv. 2014;4(56):29629–41.

5. Ilyas SI, Affo S, Goyal L, Lamarca A, Sapisochin G, Yang JD, et al. Cholangiocarcinoma—novel biological insights and therapeutic strategies. Nat Rev Clin Oncol. 2023;20(7):470–86.
6. Kelley RK, Bridgewater J, Gores GJ, Zhu AX. Systemic therapies for intrahepatic cholangiocarcinoma. J Hepatol. 2020;72(2):353–63.
7. Moris D, Palta M, Kim C, Allen PJ, Morse MA, Lidsky ME. Advances in the treatment of intrahepatic cholangiocarcinoma: an overview of the current and future therapeutic landscape for clinicians. CA Cancer J Clin. 2023;73(2):198–222.
8. Andraus W, Tustumi F, de Meira Junior JD, Pinheiro RSN, Waisberg DR, Lopes LD, et al. Molecular profile of intrahepatic cholangiocarcinoma. Int J Mol Sci. 2023;25(1):461.
9. Barner-Rasmussen N, Pukkala E, Hadkhale K, Färkkilä M. Risk factors, epidemiology and prognosis of cholangiocarcinoma in Finland. U Eur Gastroenterol J. 2021;9(10):1128–35.
10. Brindley PJ, Bachini M, Ilyas SI, Khan SA, Loukas A, Sirica AE, et al. Cholangiocarcinoma. Nat Rev Dis Prim. 2021;7(1):65.
11. Esnaola NF, Meyer JE, Karachristos A, Maranki JL, Camp ER, Denlinger CS. Evaluation and management of intrahepatic and extrahepatic cholangiocarcinoma. Cancer. 2016;122(9):1349–69.
12. Mazzaferro V, Gorgen A, Roayaie S, Droz Dit Busset M, Sapisochin G. Liver resection and transplantation for intrahepatic cholangiocarcinoma. J Hepatol. 2020;72(2):364–77.
13. Wu Q, Ellis H, Siravegna G, Michel AG, Norden BL, de la Cruz FF, et al. Landscape of clinical resistance mechanisms to FGFR inhibitors in FGFR2-altered cholangiocarcinoma. Clin Cancer Res. 2024;30(1):198–208.
14. Ali I, Alsehli M, Scotti L, Tullius Scotti M, Tsai S-T, Yu R-S, et al. Progress in polymeric nano-medicines for theranostic cancer treatment. Polymers. 2020;12(3):598.
15. Ali I, Wani WA, Khan A, Haque A, Ahmad A, Saleem K, et al. Synthesis and synergistic antifungal activities of a pyrazoline based ligand and its copper(II) and nickel(II) complexes with conventional antifungals. Microb Pathog. 2012;53(2):66–73.
16. Ruff SM, Pawlik TM. Clinical management of intrahepatic cholangiocarcinoma: surgical approaches and systemic therapies. Front Oncol. 2024;14:1321683.
17. Lee T, Teng TZJ, Shelat VG. Carbohydrate antigen 19-9—tumor marker: past, present, and future. World J Gastrointest Surg. 2020;12(12):468–90.
18. Indellicato R, Zulueta A, Caretti A, Trinchera M. Complementary use of carbohydrate antigens Lewis a, Lewis b, and Sialyl-Lewis a (CA19.9 Epitope) in gastrointestinal cancers: biological rationale towards a personalized clinical application. Cancers. 2020;12(6):1509.
19. Cuenco J, Wehnert N, Blyuss O, Kazarian A, Whitwell HJ, Menon U, et al. Identification of a serum biomarker panel for the differential diagnosis of cholangiocarcinoma and primary sclerosing cholangitis. Oncotarget. 2018;9(25):17430–42.
20. Villard C, Friis-Liby I, Rorsman F, Said K, Warnqvist A, Cornillet M, et al. Prospective surveillance for cholangiocarcinoma in unselected individuals with primary sclerosing cholangitis. J Hepatol. 2023;78(3):604–13.
21. Asaoka T, Kobayashi S, Hanaki T, Iwagami Y, Tomimaru Y, Akita H, et al. Clinical significance of preoperative CA19-9 and lymph node metastasis in intrahepatic cholangiocarcinoma. Surg Today. 2020;50(10):1176–86.
22. Yoo T, Park S-J, Han S-S, Kim SH, Lee SD, Kim Y-K, et al. Postoperative CA19-9 change is a useful predictor of intrahepatic cholangiocarcinoma survival following liver resection. Dis Mark. 2015;2015:298985.
23. Granata V, Fusco R, De Muzio F, Cutolo C, Grassi F, Brunese MC, et al. Risk assessment and cholangiocarcinoma: diagnostic management and artificial intelligence. Biology. 2023;12(2):213.
24. Li L, Wang C, Qiu Z, Deng D, Chen X, Wang Q, et al. Triptolide inhibits intrahepatic cholangiocarcinoma growth by suppressing glycolysis via the AKT/mTOR pathway. Phytomedicine. 2023;109:154575.
25. Li X, Yu C, Luo Y, Lin J, Wang F, Sun X, et al. Aldolase A enhances intrahepatic cholangiocarcinoma proliferation and invasion through promoting glycolysis. Int J Biol Sci. 2021;17(7):1782–94.
26. Chen Z, Han F, Du Y, Shi H, Zhou W. Hypoxic microenvironment in cancer: molecular mechanisms and therapeutic interventions. Signal Transduct Target Ther. 2023;8(1):70.
27. Liu Y, Zuo D, Huang C, Zhao M, Hou Y, Chang J, et al. Relationship between hypoxia and carcinoembryonic antigen and upregulated carcinoembryonic antigen is associated with poor prognosis in breast cancer patients. Clin Lab. 2019;65(12):2243–52.
28. Wang J, Wang W, Chen X, Ma D, Du G, Xia T, et al. Laparoscopic versus open hepatectomy for intrahepatic cholangiocarcinoma in patients aged 60 and older: a retrospective cohort study. World J Surg Oncol. 2022;20(1):396.
29. Jinhuan Y, Yi W, Yuanwen Z, Delin M, Xiaotian C, Yan W, et al. Laparoscopic versus open surgery for early-stage intrahepatic cholangiocarcinoma after mastering the learning curve: a multicenter data-based matched study. Front Oncol. 2021;11:742544.
30. Dong L, Lu D, Chen R, Lin Y, Zhu H, Zhang Z, et al. Proteogenomic characterization identifies clinically relevant subgroups of intrahepatic cholangiocarcinoma. Cancer Cell. 2022;40(1):70.
31. Boerner T, Drill E, Pak LM, Nguyen B, Sigel CS, Doussot A, et al. Genetic determinants of outcome in intrahepatic cholangiocarcinoma. Hepatology. 2021;74(3):1429–44.
32. Farshidfar F, Zheng S, Gingras M-C, Newton Y, Shih J, Robertson AG, et al. Integrative genomic analysis of cholangiocarcinoma identifies distinct IDH-mutant molecular profiles. Cell Rep. 2017;19(13):2878–80.
33. Ahn KS, O'Brien D, Kang YN, Mounajjed T, Kim YH, Kim T-S, et al. Prognostic subclass of intrahepatic cholangiocarcinoma by integrative molecular-clinical analysis and potential targeted approach. Hepatol Int. 2019;13(4):490–500.
34. Chaisaingmongkol J, Budhu A, Dang H, Rabibhadana S, Pupacdi B, Kwon SM, et al. Common molecular subtypes among Asian hepatocellular carcinoma and cholangiocarcinoma. Cancer Cell. 2017;32(1):57.
35. Sia D, Hoshida Y, Villanueva A, Roayaie S, Ferrer J, Tabak B, et al. Integrative molecular analysis of intrahepatic cholangiocarcinoma reveals 2 classes that have different outcomes. Gastroenterology. 2013;144(4):829–40.
36. Andersen JB, Spee B, Blechacz BR, Avital I, Komuta M, Barbour A, et al. Genomic and genetic characterization of cholangiocarcinoma identifies therapeutic targets for tyrosine kinase inhibitors. Gastroenterology. 2012;142(4):1021.
37. Xue R, Zhang Q, Cao Q, Kong R, Xiang X, Liu H, et al. Liver tumour immune microenvironment subtypes and neutrophil heterogeneity. Nature. 2022;612(7938):141–7.
38. Wu R, Guo W, Qiu X, Wang S, Sui C, Lian Q, et al. Comprehensive analysis of spatial architecture in primary liver cancer. Sci Adv. 2021;7(51):eabg3750.
39. Wu T, Hu E, Xu S, Chen M, Guo P, Dai Z, et al. clusterProfiler 4.0: a universal enrichment tool for interpreting omics data. Innovation. 2021;2(3):100141.
40. Hao Y, Hao S, Andersen-Nissen E, Mauck WM, Zheng S, Butler A, et al. Integrated analysis of multimodal single-cell data. Cell. 2021;184(13):3573.
41. Korsunsky I, Millard N, Fan J, Slowikowski K, Zhang F, Wei K, et al. Fast, sensitive and accurate integration of single-cell data with Harmony. Nat Methods. 2019;16(12):1289–96.
42. Chu Y, Dai E, Li Y, Han G, Pei G, Ingram DR, et al. Pan-cancer T cell atlas links a cellular stress response state to immunotherapy resistance. Nat Med. 2023;29(6):1550–62.
43. Patel AP, Tirosh I, Trombetta JJ, Shalek AK, Gillespie SM, Wakimoto H, et al. Single-cell RNA-seq highlights intratumoral heterogeneity in primary glioblastoma. Science. 2014;344(6190):1396–401.
44. Wu Y, Yang S, Ma J, Chen Z, Song G, Rao D, et al. Spatiotemporal immune landscape of colorectal cancer liver metastasis at single-cell level. Cancer Discov. 2022;12(1):134–53.
45. Qiu X, Mao Q, Tang Y, Wang L, Chawla R, Pliner HA, et al. Reversed graph embedding resolves complex single-cell trajectories. Nat Methods. 2017;14(10):979–82.
46. Jin S, Guerrero-Juarez CF, Zhang L, Chang I, Ramos R, Kuan C-H, et al. Inference and analysis of cell-cell communication using cell chat. Nat Commun. 2021;12(1):1088.
47. Browaeys R, Saelens W, Saeys Y. NicheNet: modeling intercellular communication by linking ligands to target genes. Nat Methods. 2020;17(2):159–62.
48. Rees MG, Seashore-Ludlow B, Cheah JH, Adams DJ, Price EV, Gill S, et al. Correlating chemical sensitivity and basal gene expression reveals mechanism of action. Nat Chem Biol. 2016;12(2):109–16.
49. Mao X, Xu J, Wang W, Liang C, Hua J, Liu J, et al. Crosstalk between cancer-associated fibroblasts and immune cells in the tumor microenvironment: new findings and future perspectives. Mol Cancer. 2021;20(1):131.
50. Li C, Teixeira AF, Zhu H-J, Ten Dijke P. Cancer associated-fibroblast-derived exosomes in cancer progression. Mol Cancer. 2021;20(1):154.

51. Yamamoto Y, Kasashima H, Fukui Y, Tsujio G, Yashiro M, Maeda K. The heterogeneity of cancer-associated fibroblast subpopulations: their origins, biomarkers, and roles in the tumor microenvironment. Cancer Sci. 2023;114(1):16–24.
52. Vassiliou E, Farias-Pereira R. Impact of lipid metabolism on macrophage polarization: implications for inflammation and tumor immunity. Int J Mol Sci. 2023;24(15):12032.
53. Tian J, Zhang L, La X, Fan X, Li A, Wu C, et al. Tumor-secreted GRP78 induces M2 polarization of macrophages by promoting lipid catabolism. Cell Signal. 2023;108:110719.
54. Qiao X, Hu Z, Xiong F, Yang Y, Peng C, Wang D, et al. Lipid metabolism reprogramming in tumor-associated macrophages and implications for therapy. Lipids Health Dis. 2023;22(1):45.
55. Yang H, Wang J, Li Z, Yang Y, Yang L, Zhang Y, et al. Risk factors and outcomes of early relapse after curative resection of intrahepatic cholangiocarcinoma. Front Oncol. 2019;9:854.
56. Li S, Balmain A, Counter CM. A model for RAS mutation patterns in cancers: finding the sweet spot. Nat Rev Cancer. 2018;18(12):767–77.
57. Kim D, Xue JY, Lito P. Targeting KRAS(G12C): from inhibitory mechanism to modulation of antitumor effects in patients. Cell. 2020;183(4):850–9.
58. Banales JM, Marin JJG, Lamarca A, Rodrigues PM, Khan SA, Roberts LR, et al. Cholangiocarcinoma 2020: the next horizon in mechanisms and management. Nat Rev Gastroenterol Hepatol. 2020;17(9):557–88.
59. Zhou S-L, Xin H-Y, Sun R-Q, Zhou Z-J, Hu Z-Q, Luo C-B, et al. Association of KRAS variant subtypes with survival and recurrence in patients with surgically treated intrahepatic cholangiocarcinoma. JAMA Surg. 2022;157(1):59–65.
60. Bartman CR, Weilandt DR, Shen Y, Lee WD, Han Y, TeSlaa T, et al. Slow TCA flux and ATP production in primary solid tumours but not metastases. Nature. 2023;614(7947):349–57.
61. Chae H-S, Hong S-T. Overview of cancer metabolism and signaling transduction. Int J Mol Sci. 2023;24(1):12.
62. Yadav D, Yadav A, Bhattacharya S, Dagar A, Kumar V, Rani R. GLUT and HK: two primary and essential key players in tumor glycolysis. Semin Cancer Biol. 2024;100:17–27.
63. Zheng X, Fan H, Liu Y, Wei Z, Li X, Wang A, et al. Hypoxia boosts aerobic glycolysis in carcinoma: a complex process for tumour development. Curr Mol Pharmacol. 2022;15(3):487–501.
64. Zhang Y, Zhang X, Meng Y, Xu X, Zuo D. The role of glycolysis and lactate in the induction of tumor-associated macrophages immunosuppressive phenotype. Int Immunopharmacol. 2022;110:108994.
65. Singh L, Nair L, Kumar D, Arora MK, Bajaj S, Gadewar M, et al. Hypoxia induced lactate acidosis modulates tumor microenvironment and lipid reprogramming to sustain the cancer cell survival. Front Oncol. 2023;13:1034205.
66. Romero-Garcia S, Moreno-Altamirano MMB, Prado-Garcia H, Sánchez-García FJ. Lactate contribution to the tumor microenvironment: mechanisms, effects on immune cells and therapeutic relevance. Front Immunol. 2016;7:52.
67. Guedj N, Blaise L, Cauchy F, Albuquerque M, Soubrane O, Paradis V. Prognostic value of desmoplastic stroma in intrahepatic cholangiocarcinoma. Mod Pathol. 2021;34(2):408–16.
68. Job S, Rapoud D, Dos Santos A, Gonzalez P, Desterke C, Pascal G, et al. Identification of four immune subtypes characterized by distinct composition and functions of tumor microenvironment in intrahepatic cholangiocarcinoma. Hepatology. 2020;72(3):965–81.
69. Barba I, Carrillo-Bosch L, Seoane J. Targeting the warburg effect in cancer: where do we stand? Int J Mol Sci. 2024;25(6):3142.
70. Shang R-Z, Qu S-B, Wang D-S. Reprogramming of glucose metabolism in hepatocellular carcinoma: progress and prospects. World J Gastroenterol. 2016;22(45):9933–43.
71. Madden MZ, Rathmell JC. The complex integration of T-cell metabolism and immunotherapy. Cancer Discov. 2021;11(7):1636–43.
72. Chou M-Y, Yang M-H. Interplay of immunometabolism and epithelial-mesenchymal transition in the tumor microenvironment. Int J Mol Sci. 2021;22(18):9878.
73. Ho K-H, Huang T-W, Shih C-M, Lee Y-T, Liu A-J, Chen P-H, et al. Glycolysis-associated lncRNAs identify a subgroup of cancer patients with poor prognoses and a high-infiltration immune microenvironment. BMC Med. 2021;19(1):59.
74. Zaarour RF, Ribeiro M, Azzarone B, Kapoor S, Chouaib S. Tumor microenvironment-induced tumor cell plasticity: relationship with hypoxic stress and impact on tumor resistance. Front Oncol. 2023;13:1222575.
75. Liao C, Liu X, Zhang C, Zhang Q. Tumor hypoxia: from basic knowledge to therapeutic implications. Semin Cancer Biol. 2023;88:172–86.
76. Ciepła J, Smolarczyk R. Tumor hypoxia unveiled: insights into microenvironment, detection tools and emerging therapies. Clin Exp Med. 2024;24(1):235.
77. Dobosz P, Dzieciątkowski T. The intriguing history of cancer immunotherapy. Front Immunol. 2019;10:2965.
78. Gao J-H, Wang C-H, Tong H, Wen S-L, Huang Z-Y, Tang C-W. Targeting inhibition of extracellular signal-regulated kinase kinase pathway with AZD6244 (ARRY-142886) suppresses growth and angiogenesis of gastric cancer. Sci Rep. 2015;5:16382.
79. Morelli MP, Tentler JJ, Kulikowski GN, Tan A-C, Bradshaw-Pierce EL, Pitts TM, et al. Preclinical activity of the rational combination of selumetinib (AZD6244) in combination with vorinostat in KRAS-mutant colorectal cancer models. Clin Cancer Res. 2012;18(4):1051–62.
80. Subbiah V, Lassen U, Élez E, Italiano A, Curigliano G, Javle M, et al. Dabrafenib plus trametinib in patients with BRAFV600E-mutated biliary tract cancer (ROAR): a phase 2, open-label, single-arm, multicentre basket trial. Lancet Oncol. 2020;21(9):1234–43.

Publisher's Note